Evolution of Jupiter-style critical latitudes: Initial laboratory altimetry results

Y.D. Afanasyev[1], T.E. Dowling[2]

[1]Department of Physics & Physical Oceanography, Memorial University of Newfoundland, St. John's, Newfoundland and Labrador, Canada
[2]Department of Physics & Astronomy, University of Louisville, Louisville KY, USA 40292

Key Points:

- Stability of jets is assured when critical latitudes (extrema of potential vorticity) are "supersonic" with respect to Rossby waves.
- Multiple stable critical latitudes on Jupiter and Saturn motivate this study of a rotating water tank with two built-in critical latitudes.
- Lab altimetry records alternating jets forming from local forcing and distinguishes between Jupiter-like and non-Jupiter-like environments.

Corresponding author: Y.D. Afanasyev, afanai@mun.ca

Abstract

This is a laboratory zonal-jet study using a rotating water tank. The bottom topography has a tent-shaped radial cross section designed to generate two critical latitudes, i.e. two positions where β_e, the radial gradient of the potential vorticity (PV), changes sign. This configuration is motivated by observations indicating Jupiter and Saturn have not only multiple zonal jets, but multiple stable critical latitudes. It is known that "supersonic" critical latitudes (with respect to Rossby waves) are stable, whereas "subsonic" critical latitudes are posited to be unstable. Because Rossby waves are uni-directional, "supersonic" critical latitudes come in two varieties: Rossby Mach number $M_{\mathrm{R}} > 1$ and $M_{\mathrm{R}} < 0$, where the latter holds when the waves are directed downstream. Experiments focus on: i) how do zonal jets emerge from localized forcing in a system with alternating PV gradients? and ii) what differences are there between the evolution of various types of critical latitudes? The water is forced by mass injection along one radius. Laboratory altimetry provides accurate, unobtrusive records of the circulations that reveal the emergence of counter-propagating β-plumes (Rossby-wave envelopes), which expand into tank-encircling zonal jets. The tank's negative β_e annulus is characterized by $M_{\mathrm{R}} \sim 1$, which is the condition surmised for Jupiter and Saturn. The weaker critical latitude (in terms of jumps in the PV-gradient) adjusts its position by $\sim 4\%$ of the tank radius and maintains $M_{\mathrm{R}} \sim 1$. In contrast, the stronger one vacillates while maintaining $|M_{\mathrm{R}}| \ll 1$, and may be relevant to steep oceanic seamounts.

Plain Language Summary

Jupiter is striped with dark and light bands called belts and zones, which are associated with its steady eastward and westward jet streams ("jets" for short). Entwined within these are long waves that would cause the jets to meander and buckle, like Earth's jet streams do, were it not for guide rails that are buried inside the gas giant: the steady pressure ridges and troughs, called dynamic topography, that are associated with the planet's abyssal jets. This work employs an optical altimetry method for measuring the circulations in a rotating water tank without disturbing the flow. The tank's bottom topography is a tent-shaped peak that encircles the tank like a doughnut and provides a Jupiter-style guide rail. The flow is forced by injecting water from the holes of a submerged pipe that extends along one radius. Many different types of waves are recorded propagating away from this forcing, and the circulations are seen to evolve into alternating eastward and westward jets that encircle the tank. Where long waves travel upstream at about the same rate as the flow itself travels downstream, such that the waves are approximately stationary, the system exhibits Jupiter-like characteristics.

1 Introduction

Jet streams ("jets" for short) play a guiding role in atmospheric and oceanic fluid dynamics, and have analogies across many disciplines, including jets in magnetized plasmas and in protoplanetary disks (Baldwin et al., 2007; Dowling, 2019). Jupiter's jets are the prototypical system: the first hint of order out of chaos came from the discovery of the planet's belts in 1630 (Graney, 2010). The jets are beautifully structured and provide counterpoints to atmospheric turbulence, as evident in high-resolution imagery from Pioneer 10 and 11, Voyager 1 and 2, Galileo, Juno, Cassini-Huygens and New Horizons. The flow visualization of Jupiter's cloud tops rivals that which can be achieved in the laboratory, permitting detailed analysis of velocity and vorticity fields. This has revealed that Jupiter's troposphere is composed of not only multiple stable jets, but of multiple stable critical latitudes (Dowling & Ingersoll, 1989; Dowling, 1993, 1995b; Read et al., 2006). This appears to also hold for Saturn (Read, Conrath, et al., 2009; Read, Dowling, & Schubert, 2009). The inference that gas giants have multiple stable critical latitudes is the primary motivation for the class of laboratory experiments initiated here.

1.1 Multiple stable critical latitudes

In the context of inviscid shear stability, a critical latitude (also known as a critical line, critical surface, or critical layer) marks the position of a local extremum in potential vorticity (PV), where the gradient of the PV changes sign. Rossby wave phase speeds (before advection by the wind) travel with high PV on their right—they are uni-directional—hence a critical latitude marks a pivot point for the direction of propagation, which has a governing effect on the fluid dynamics. "Supersonic" critical latitudes are proven to be stable (the quotes indicate the discussion is about Rossby waves, not sound waves), via the two branches of Kelvin-Arnol'd shear stability theory (KA-I and KA-II) cast in non-dimensional form (McIntyre & Shepherd, 1987; Dowling, 2014). The Rayleigh, Kuo, Charney-Stern, and Fjørtoft stability criteria are special cases of the KA-I branch, and interestingly, both branches are "supersonic": KA-II corresponds to the usual $M_\mathrm{R} > 1$, where M_R is the analog of the Mach number, and KA-I corresponds to $M_\mathrm{R} < 0$, which stems from the uni-directionality of Rossby waves and holds when their longwave speeds are directed downwind. This M_R point of view is shedding new light on the classic problem of inviscid shear stability, where the lack of physical insights has long been cited as a deterrent to progress (e.g. Lin, 1945; Darrigol, 2005). The compact statement that "supersonic" critical latitudes are stable has a straightforward physical interpretation: vortical eddies, which must lean into the shear to be self-amplifying, are relentlessly toppled downstream and thus rendered self-damping (see Figures 5 and 6 in Dowling, 2014). Likewise, an open conjecture posits that "subsonic" critical latitudes are unstable, which has numerical support (e.g. Dowling, 1993; Stamp & Dowling, 1993; Dowling, 2020) but has not yet been proven mathematically.

Systems containing a single stable critical latitude have been well studied (e.g. Kuo, 1949; Balmforth & Morrison, 1999; Hirota & Morrison, 2016), including applications to rotating water tank experiments (e.g. del Castillo-Negrete & Morrison, 1993). The more complicated case of multiple stable critical latitudes is "possibly the most interesting" (Balmforth & Morrison, 2002, p. 138), but is less-well studied and so there is much that laboratory experiments can contribute. Three questions immediately present themselves. Firstly, the existence of multiple critical latitudes means that Rossby wave propagation switches direction where the sign of the PV gradient switches. In such an environment, how do jets spin up and stabilize? Secondly, how do the various kinds of critical latitudes evolve? Thirdly, when there is only one critical latitude, it dictates the reference frame, but when there is more than one, some type of special communication must occur in order to have the zonal wind be zero at each latitude where the PV gradient is zero. Physically, this corresponds to long Rossby waves being stationary and coherent across alternating jets. There is evidence that such coherence occurs in the tropospheres of Jupiter and Saturn (Deming et al., 1989; Dowling, 1995a; Read, Dowling, & Schubert, 2009). The first two questions, how jets evolve and how different kinds of critical latitudes behave, are directly addressed in this study.

1.2 Laboratory experiments on zonal jets

Azimuthal jets have been studied in rotating-tank laboratory experiments under a variety of configurations for decades, as recently reviewed by Read (2019) and Y. D. Afanasyev (2019). Two key distinguishing characteristics are: i) the techniques used to measure the circulations, and ii) the manner of forcing used to drive the flow.

1.2.1 Measuring the circulations

The present experiments are barotropic in the vertical dimension, in the sense that only one rapidly-rotating, incompressible layer of water is used. Vertically varying (baroclinic) structures are suppressed by the gyroscopic Taylor-Proudman effect (Vallis, 2017) and so there is little need to try to measure them (there are effective means for deduc-

ing them in rotating tanks that contain stratified fluids, which will come into play in future experiments of this type). Measuring the circulations in a single layer can be done accurately when the fluid is rapidly rotating, by measuring the highs and lows of the water's surface elevation, which are strongly coupled to the circulations via geostrophy, the balance between Coriolis accelerations and horizontal pressure gradients.

The practical challenge when monitoring rotating tank experiments is to extract as much information as possible, while disturbing the flow as little as possible. The optical altimetry technique is used in this study to precisely determine the surface elevation remotely, without introducing any disturbances to the flow (Y. D. Afanasyev et al., 2009; Y. D. Afanasyev, 2015). The surface is illuminated with a bright computer monitor located above the surface of water. The monitor displays a color pattern resembling a color wheel used by painters. Primary colors at the periphery of the pattern combine in its center into white. The pattern is reflected as white where the spun-up water is an undisturbed parabola, but otherwise is reflected as one hue or another depending sensitively on the slope and orientation of the surface anomaly (this technique is adopted from the telescope-mirror manufacturing industry). Gradient-wind balance is then used to invert this slope altimetry into high-resolution velocity and vorticity fields. The images are taken with a video camera that yields temporal resolution that is sufficient to discern the different propagation characteristics of all the wave types of interest, and to record the long-term evolution of jets.

1.2.2 Forcing

There are about as many schemes for forcing as there are world-wide laboratories engaged in rotating-tank experiments. A system's reactions can be divided into those that are independent of the forcing type, and those that are a signature of the particular forcing employed. Quite uniform small-scale forcing can be achieved thermally via evaporative cooling of warm water, which creates small-scale convective vortices. Condie and Rhines (1994) observed jets forming from this type of forcing, and Matulka et al. (2016) did the same by combining this technique with heating at the bottom. An alternative is to employ the second half of oceanography's thermohaline driver, the haline/saline half, for example Read et al. (2019) sprayed salty water on the surface to generate small-scale convective motions and observe jet formation.

In addition to thermohaline techniques, one can also generate jets by perturbing the momentum or mass fields in a tank. A straightforward example of the former is to have sliding concentric rings on the bottom (e.g. Antipov et al., 1983). Various tanks employ the latter by pumping water in and out of holes arrayed in patterns at the bottom (e.g. Sommeria et al., 1989). Since zonal jets are large-scale phenomena, there are some advantages to using azimuthally localized forcing that is much smaller in scale than the resultant jets, which is the technique employed here. In this approach, fluid is pumped into the tank in a localized area, often along a single radius. Either the same or different density from the fluid in the tank can be used, which results in barotropic or baroclinic circulations, respectively. Using this approach, Y. D. Afanasyev et al. (2012) and Slavin and Afanasyev (2012) observed zonal jets forming out of the growing envelope of Rossby waves emitted from the local forcing, called the β-plume mechanism.

Although small-scale convective forcing is arguably more relevant to modelling planetary atmospheres, in this study the azimuthally localized, same-density mass injection technique is used, which permits β-plumes to expand into an otherwise unforced domain. This is advantageous for studying how β-plumes grow into zonal jets when the system has adjacent zones with alternating signs of the PV gradient, such that the Rossby-wave propagation direction alternates.

1.2.3 Bottom topography

The PV gradient has three components on a rotating planet, which arise from changes with respect to latitude of the planetary, relative, and stretching vorticities. The planetary vorticity gradient is $\beta = df/dy$, where $f = 2\Omega\sin(\phi_g)$ is the planetary vorticity or Coriolis parameter, Ω is the sidereal angular velocity of the planet's rotation, ϕ_g is the planetographic latitude, and y is the local Cartesian latitude coordinate. The β term has the feature that it is positive in both the northern and southern hemispheres (zero at the poles), and has played an important role in the theory of Rossby waves (Platzman, 1968). Although β is difficult to reproduce in the laboratory, where rotating tanks usually have a cylindrical geometry instead of a spherical-shell geometry (a notable exception is the microgravity convection apparatus deveolped by Hart et al., 1986), its absence in rotating tanks is of little concern, for at least two reasons. Firstly, the fluid cannot cherry-pick β out of the full PV gradient, so as long as one or both of the other two terms yields a non-zero PV gradient, there is no awareness in the system that $\beta = 0$. Secondly, on Jupiter and Saturn the alternating jets are so strong that the relative vorticity and stretching vorticity gradients are two to three times larger in magnitude than β (Ingersoll et al., 1981; Dowling, 2020), implying that β itself could be turned off without strongly affecting the dynamics.

The primary method for arranging a background PV gradient in a rotating tank is to configure the depth of the water to change with respect to radius, which causes gradients in the stretching vorticity and hence the PV. Variations in depth are due to a combination of bottom topography and the parabolic shape of the free surface of the rotating water, plus any perturbations. While in previous laboratory experiments the resulting PV gradients have typically been single-signed across the domain, here a bottom topography is employed that creates zones that alternate from positive to negative back to positive PV gradient with respect to radius. This builds in two critical latitudes (critical radii) where the PV gradient changes sign.

The rest of the article is organized as follows. Section 2 reviews pertinent advances in the theory of Rossby waves, jets, and their interactions. In particular, the reciprocal of the analog of the Mach number for Rossby waves is highlighted as a unifying dimensionless parameter. Section 3 contains details of the laboratory apparatus and the optical altimetry system. Section 4 describes the results of the experiments, and Section 5 gives concluding remarks.

2 Theory

Jet streams are inextricably linked with shear and vorticity—vortical flow—and vorticity waves, which are called Rossby waves in geophysical fluid dynamics and drift waves in plasma dynamics, are central to the genesis and maintenance of jets (Galperin & Read, 2019; Dowling, 2019). Rossby waves are the result of fluid parcels conserving their PV in the presence of an environmental PV gradient (Vallis, 2017), hence the sign and magnitude of PV gradients are controlling factors in the development of jets.

2.1 Rossby waves and critical latitudes

The central evolution equation for inviscid, adiabatic, and hydrostatic flow is conservation of PV (symbol Q), which is formed by combining the conservation laws of mass, momentum and thermal energy to yield (in the primitive Ertel form):

$$\frac{dQ}{dt} = 0\,; \qquad Q = \frac{f+\zeta}{h}\,, \tag{1}$$

where f is the aforementioned planetary vorticity (the Coriolis parameter), ζ is the local vertical component of the relative vorticity (relative to the rotating frame of refer-

ence), and h is the fluid depth of the water (the distance from the bottom topography to the water's surface), or for atmospheres the thickness density of the air (Vallis, 2017).

2.1.1 Meridional gradient of PV

For most systems, the meridional component of the gradient of the PV is the largest and most important. It is expressed here for clarity in the Cartesian framework,

$$Q_y = \frac{1}{h}(f_y + \zeta_y) - \frac{h_y}{h^2}(f + \zeta)\,, \tag{2}$$

where subscripts denote differentiation. For zonally symmetric flow the relative vorticity is $\zeta = -u_y$, and the product hQ_y may be written

$$hQ_y \equiv \beta_e = \beta + \beta_u + \beta_h\,, \tag{3}$$

where β_e is the mass-weighted PV gradient ("e" for "effective"), $\beta = f_y$ is the planetary vorticity gradient, $\beta_u = \zeta_y = -u_{yy}$ is the relative vorticity gradient, and

$$\beta_h = -f\frac{h_y}{h}\left(1 - \frac{u_y}{f}\right)\,, \tag{4}$$

is the stretching vorticity gradient.

2.1.2 Height, thickness, and the geoid

Following standard notation for interface heights and layer thicknesses (e.g. Vallis, 2017, p. 106), the zero for lab-based altitude is at or near the average of the tank's bottom topography, and η and η_b are the respective altitudes of the water surface and bottom topography, such that the water thickness is $h = \eta - \eta_b$. When the tank is not spinning, the surface is flat and its altitude equals its average thickness, h_0. After the tank is spun up, but otherwise undisturbed, the radial pressure-gradient force balances the centrifugal acceleration such that the surface is parabolic; this furnishes the system's reference geoid,

$$\eta_{\text{geoid}}(r) = h_0 + \frac{(\Omega R)^2}{2g}\left[\left(\frac{r}{R}\right)^2 - \frac{1}{2}\right]\,, \tag{5}$$

where g is the acceleration of gravity, Ω is the angular velocity of the tank, R is the tank radius, and r is the radial coordinate measured from the center (Figure 1). One could equally well define the geoid in terms of the corresponding geopotential, $\Phi_{\text{geoid}} = g\eta_{\text{geoid}}$, but the slope of η itself is what is measured by the laboratory altimetry system.

There are two different definitions of "horizontal" motion relevant to a rotating tank, and to minimize confusion it is important to explicitly pick one. One is translation parallel to the laboratory floor, which is perpendicular to both Earth's gravity and to the angular velocity vector of the rotating tank. The other is translation parallel to the water's geoid, which is perpendicular to the effective gravity (the net sum of Earth's gravity and the centrifugal acceleration of the rotating tank), which, for example, a water bug standing on the surface would deem to be sensible. In this article, the former is used: horizontal motion and horizontal velocities refer to translation parallel to the laboratory floor. The primary reason for this choice is the gyroscopic Taylor-Proudman effect, which causes the bulk circulations in a rapidly rotating incompressible fluid to translate as coherent columns that are parallel to the rotation axis (Vallis, 2017). Thus, surface-height disturbances relative to the geoid are measured using lab-vertical altitude, not local geopotential height (i.e. not the geopotential divided by a constant reference gravity, g_0), and are denoted $\eta - \eta_{\text{geoid}} = \Delta\eta$. Ignoring viscous boundary layers, the system under study is barotropic (has only one layer) and so behaves largely in a two-dimensional manner. The bottom topography in this study is zonally (azimuthally) symmetric, $\eta_b = \eta_b(r)$, and the surface height can be conveniently decomposed as either $\eta(r,\theta) = h(r,\theta) + \eta_b(r)$ or as $\eta(r,\theta) = \Delta\eta(r,\theta) + \eta_{\text{geoid}}(r)$, where θ is the azimuthal angle.

2.1.3 Quasi-geostrophic limit

The asymptotic limit of rapid rotation and strong stratification leads to the quasi-geostrophic version of β_e (sometimes written q_y). Complete derivations of quasi-geostrophic theory are given in geophysical fluid dynamics textbooks (e.g. Vallis, 2017), so here we restrict to a brief summary of the basics to be clear about the various contributions to β_e, which figure into the design of experiments. What makes the quasi-geostrophic limit particularly tractable is that both the momentum and mass fields are expressed in terms of the same streamfunction, which in this system is proportional to $\Delta\eta$. This simplifies the analysis because it leads to a single equation in a single unknown. Consider in turn each of the three terms on the right-hand side of the PV gradient (3). The first is simple: the planetary vorticity gradient, β, is unmodified in the quasi-geostrophic limit. The relevant approximations associated with β are that it is often assumed to be constant, and that it usually appears in the context of local Cartesian geometry (the β-plane approximation).

For the meridional gradient of the relative vorticity, β_u, consider that in a rapidly rotating fluid, the horizontal pressure-gradient force and the Coriolis force are nearly in balance, called geostrophic balance, such that the mass and momentum (pressure and velocity) fields are strongly coupled. Consequently, a useful way to write the lab-horizontal pressure-gradient force is to define the lab-horizontal geostrophic velocity, which for a layer of water may be written in Cartesian form,

$$(u_g,\, v_g) = \frac{g}{f_0}(-\Delta\eta_y,\, \Delta\eta_x)\,. \tag{6}$$

A key small parameter in quasi-geostrophic theory is the dimensionless Rossby number, $\mathrm{Ro} = U/(f_0 L)$, where U and L are representative horizontal speed and length scales, respectively. A rapidly rotating fluid satisfies $\mathrm{Ro} \ll 1$, and the magnitude of Ro indicates the relative error between (u_g, v_g) and the actual horizontal velocity, (u, v). This coupling (which is made more accurate below) is the general principle behind determining circulations via remote-sensing altimetry.

The geostrophic velocity has zero divergence, $(u_g)_x + (v_g)_y = 0$, and its relative vorticity is related to $\Delta\eta$ via a horizontal Laplacian,

$$\zeta \approx \zeta_g = (v_g)_x - (u_g)_y = \frac{g}{f_0}\left(\Delta\eta_{xx} + \Delta\eta_{yy}\right)\,. \tag{7}$$

(Note that in this notation, the "Δ" symbol is not the Laplacian, rather the subscript partial derivatives are.) For zonally symmetric flow in the quasi-geostrophic limit, (7) implies that the relative-vorticity gradient is approximately equal to the third derivative of the height anomaly, multiplied by g/f_0,

$$\beta_u = -u_{yy} \approx \frac{g}{f_0}\Delta\eta_{yyy}\,. \tag{8}$$

A streamfunction is often introduced to simplify the notation, $\psi = (g/f_0)\Delta\eta$, but again since $\Delta\eta$ is directly measured by the laboratory altimetry method, in this article the relevant expressions are mostly maintained in terms of $\Delta\eta$.

For the meridional gradient of the stretching vorticity, β_h, consider that for the case of rapid rotation, Ro approaches zero and thus the factor $(1 - u_y/f) \sim (1 \pm \mathrm{Ro})$ approaches unity, such that (4) becomes

$$\beta_h \approx -\frac{f_0}{h}h_y = \frac{1}{L_d^2}\left(-\frac{g}{f_0}h_y\right)\,,$$

where $L_d^2 = gh/f_0^2$ is the square of the deformation length, an important intrinsic length scale in rotating-fluid systems. Since $h = \eta_{\mathrm{geoid}} + \Delta\eta - \eta_b$, such that $h_y = \Delta\eta_y +$

$(\eta_{\rm geoid} - \eta_b)_y$, the geostrophic current (6) replaces $-(g/f_0)\Delta\eta_y$ to yield

$$\beta_h \approx \frac{1}{L_d^2}\left(u_g - \frac{g}{f_0}\left(\eta_{\rm geoid} - \eta_b\right)_y\right) . \tag{9}$$

For application to planetary systems, where the definition of horizontal is in the geopotential sense for which $(\eta_{\rm geoid})_y = 0$, then the remaining η_b term in (9) is interpreted as the dynamic topography of deep jets (Ingersoll & Cuong, 1981; Dowling, 2020); alternatively, when the definition of horizontal is in the lab sense as in this article, then the combination $(\eta_b - \eta_{\rm geoid})$ serves the same purpose.

2.1.4 Rossby waves

Rossby waves largely govern the formation and evolution of jets, which is a leading reason that alternating PV gradients are interesting. Phillips (1965) analyzed, in cylindrical geometry, Rossby waves arising from the stretching-vorticity gradient associated with the parabolic geoid of a rotating water tank. Staying for the moment in Cartesian geometry, conservation of PV is

$$dq/dt = 0 \quad \Rightarrow \quad q_t + (u-\alpha)q_x + vq_y = 0\,. \tag{10}$$

The term α is a built-in Galilean reference-frame shift, which will prove useful below when analyzing critical latitudes (note that q itself is Galilean invariant). Rossby waves are found by linearizing (10) about a basic state. Consider a zonally symmetric profile, $u = \overline{u}(y) + u'$, $v = v'$, and $q = \overline{q} + q'$, which yields

$$q'_t + (\overline{u} - \alpha)q'_x + v'\,\overline{q}_y = 0\,. \tag{11}$$

In the quasi-geostrophic limit, all the perturbations in (11) can be expressed in terms of a single variable, the eddy surface height relative to the geoid, η', which is defined in the same manner as $\Delta\eta$, but is written with a prime to signal that only small-amplitude perturbations are being considered.

Working on (11) from right to left, the meridional velocity is $v' = (g/f_0)\eta'_x$. The environmental PV gradient, $\overline{q}_y \equiv \beta_e(y)$, is a given profile and in general is one of the two non-constant coefficients of the differential equation. If β is the dominant component of β_e, then this is an approximately constant coefficient, as it is often assumed to be in introductory textbooks (e.g. Cushman-Roisin & Beckers, 2011). However, jets by their nature are associated with non-negligible values of β_u (barotropic jets) and/or β_h (baroclinic jets). These change as the jets evolve, and generally render $\beta_e(y)$ to not be a constant coefficient. Considering that the fluid cannot pick β or β_u or β_h, but only reacts to their sum, β_e, it is important to focus on the latter (see the discussion on the Rhines length below). Moving to the middle of (11), the zonal wind, $\overline{u}(y) - \alpha$, is also a given profile and is also a non-constant coefficient where there are jets, by definition. Fortunately, $\overline{q}_y$ and $(\overline{u}-\alpha)$ are usually correlated in Nature (Dowling, 1993; Read et al., 2006; Read, Conrath, et al., 2009; Read, Dowling, & Schubert, 2009; Du et al., 2015; Dowling et al., 2017; Stanley et al., 2020).

The remaining factors in (11) are q'_x and q'_t. The eddy relative vorticity in (7), together with the stretching vorticity implicit in the gradient (9), imply

$$q'_x = \frac{g}{f_0}\left(\eta'_{xxx} + \eta'_{yyx} - L_d^{-2}\eta'_x\right) , \tag{12}$$

$$q'_t = \frac{g}{f_0}\left(\eta'_{xxt} + \eta'_{yyt} - L_d^{-2}\eta'_t\right) . \tag{13}$$

To proceed to analytical results for non-constant coefficient cases, one can limit the variation of the coefficients (meaning the variation of the jets) and work in the WKBJ

framework (e.g. Young & Rhines, 1980), or proceed in terms of a series or Galerkin framework customized to the particular case in hand, such as a sinusoidal jet (e.g. Stamp & Dowling, 1993). Short of this, and as a step towards building intuition for the fully nonlinear experiments, consider the textbook case when β_e and L_d are constant and the boundary conditions are periodic, so that one can assume sinusoidal perturbations for Cartesian geometry, $\eta' \propto \exp[i(kx + ly - \omega t)]$, such that $\partial/\partial t \rightarrow -i\omega$, $\partial/\partial x \rightarrow ik$, and $\partial/\partial y \rightarrow il$. Conservation of quasi-geostrophic PV in terms of η' then yields the following dispersion relation for Rossby waves (Vallis, 2017)

$$\omega(k,l) = (\overline{u} - \alpha)k - \frac{\beta_e k}{k^2 + l^2 + L_d^{-2}} \quad (\text{constant } \overline{u},\, \beta_e,\, L_d)\,. \tag{14}$$

The intrinsic zonal phase speed (before Doppler shifting), $\hat{c}_x = \omega/k - (\overline{u} - \alpha)$, is

$$\hat{c}_x = -\beta_e L_d^2\,(1 + \mathrm{Bu})^{-1} \quad (\text{constant coeffs.})\,, \tag{15}$$

where $\mathrm{Bu} = (k^2 + l^2)L_d^2$ is the wave Burger number, which can be interpreted as the non-dimensional squared deformation length associated with a given wavenumber, or vice versa.

Significantly, there also exists a non-constant coefficient special case: when β_e and $(\overline{u} - \alpha)$ are strictly proportional to each other, such that $\beta_e = \kappa^2(\overline{u} - \alpha)$ for some proportionality constant, κ^2. In other words, the jets in this case can be zigzaggy like Jupiter's, so long as the PV gradient is equally zigzaggy. In the steady-state limit, $q'_t = 0$ in (11) and the non-constant coefficients then cancel out, leaving

$$\frac{\partial}{\partial x}\left(q' + \kappa^2 \psi'\right) = 0\,, \tag{16}$$

where the streamfunction notation has been brought in for convenience, $v' = (g/f_0)\eta'_x = \psi'_x$. Apart from an innocuous outer x derivative, (16) is simply the eigenvalue problem connecting the eddy PV to the eddy streamfunction. The corresponding eigenfunctions are steady, and they extend coherently across the alternating jets without being sheared (Stamp & Dowling, 1993; Dowling, 2019). While the present experiments are not optimized to study this phenomenon, it is a long-term goal.

2.1.5 Critical latitudes

Recall that latitudes where Rossby waves change direction relative to the flow are called critical latitudes, and correspond to locations where $\hat{c}_x$ changes sign, which from (15) correspond to where β_e changes sign. Critical latitudes have major implications for the dynamics of jets, including wave transmission and absorption (Vallis, 2017). The magnitude of the intrinsic phase speed is fastest in the longwave limit, $\mathrm{Bu} \rightarrow 0$, and in this limit the phase speed and the group velocity both asymptote to the same value, $-\beta_e L_d^2$, such that long Rossby waves are non-dispersive (Hide, 1969). Both these facts make it straightforward to define and work with the analog of the Mach number for Rossby waves, as discussed below. From the M_{R} point of view, analyzing shear stability proceeds by first finding all the critical latitudes in a system, and then classifying each as "supersonic", "sonic", or "subsonic". Only systems with "subsonic" critical latitudes can develop shear instability.

A "giant' domain (like Jupiter, Saturn, or Earth's oceans) corresponds to one for which there is sufficient room to take $Bu \rightarrow 0$ (Earth's atmosphere is not particularly giant in this regard). An intriguing question arises with multiple critical latitudes: are the longest Rossby waves confined meridionally between them, such that Bu cannot be reduced to zero and the gravest waves remain dispersive? Or instead, is the basic state able to configure itself so that the gravest waves extend coherently across critical lines, without being sheared? As alluded to above, there is empirical evidence that the latter

occurs on Jupiter (e.g. Deming et al., 1989) and Saturn (e.g. Read, Dowling, & Schubert, 2009), and numerical work that suggests such slowly-moving long waves are the hallmark of alternating zonal jets that are close to marginal shear stability (Stamp & Dowling, 1993).

2.2 Analog of the Mach number for Rossby waves, M_{R}

Since the 19$^{\mathrm{th}}$ century, for compressible and hydraulic circulations the upstream flow of information via sound waves and buoyancy waves has respectively been characterized by the dimensionless Mach and Froude numbers. A generic Mach-type number defined for flow in the x direction takes the form $u/(-\hat{c}_x)$, such that $-\hat{c}_x$ is the same sign as u for upstream waves (which are the implicit choice for omni-directional waves like sound waves and buoyancy waves). The sum $c_x = u + \hat{c}_x$ is the net wave speed after advection by the flow (after Doppler shifting). Generally, $\hat{c}_x$ is Galilean invariant, whereas u is not, hence a Mach-type field will change depending on the reference frame. Unlike sound waves and buoyancy waves, Rossby waves are uni-directional, which means that $-\hat{c}_x$ has the opposite sign to u in locations where the waves point downstream (have high PV on the right looking downstream).

In general, the analog of the Mach number for Rossby waves is

$$M_{\mathrm{R}} = \frac{u}{-\hat{c}_x} = \frac{-\psi_y}{\beta_e \kappa^{-2}} \to -\kappa^2 \frac{\partial \psi}{\partial q}\,, \tag{17}$$

where ψ is the streamfunction. The rightmost expression in (17) relaxes the assumption of zonal symmetry. Notice that the sign of M_{R} is always opposite to the sign of the correlation between the streamfunction and PV. When working with field data, this streamfunction-vorticity correlation is determined via a local linear regression (Du et al., 2015; Dowling et al., 2017; Stanley et al., 2020). Negative M_{R} corresponds to the case when the long Rossby waves are directed downstream and consequently information flows downstream regardless of the flow speed, with no possibility of standing or upstream-directed waves. This $M_R < 0$ case is a second form of "supersonic" flow that arises only for uni-directional waves (i.e. not sound waves or gravity waves).

2.2.1 M_{R} and eastward currents

One of the earliest mentions of M_{R} appears in Long (1952) as part of an analysis of experiments using a rotating hemispherical shell that is orientated like a bowl and filled with water. An obstacle representing a mountain or seamount barrier is moved either slightly more slowly or slightly more quickly than the shell, such that in the obstacle's reference frame there is either a fairly uniform eastward or westward (prograde or retrograde) current, respectively. The form of M_{R} considered is $V/\beta L^2$, where V and L are characteristic horizontal velocity and length scales, respectively (Long, 1952, p. 195). Although $V/\beta L^2$ is not explicitly treated as a signed quantity in this early paper, it is done so implicitly since $\beta_e \approx \beta$ is positive and one of the main results of the work is the existence of standing long Rossby waves for eastward currents ($V > 0$, $M_{\mathrm{R}} \sim 1$) and their absence for westward currents ($V < 0$, $M_{\mathrm{R}} < 0$).

The theme of fairly uniform eastward currents, for which both β_u and β_h in (3) are negligible compared to β, so that $\beta_e \to \beta$ and $M_{\mathrm{R}} > 0$, has continued to be pursued by several groups. In these studies, M_R is generally treated as a positive constant, rather than as a field variable. Fultz (1961, p. 67) gives $V/\beta L^2$ the name β-Rossby number, denotes it $R^*_{0\beta}$, and points out its dynamical equivalence to the Froude number that arises in two-dimensional stratified flow. White (1971) studies the wake of an eastward current past a cylindrical island with radius a, defines an island number, $\mathrm{Is} = (\beta a^2/U)^{1/2}$ — which is $M_{\mathrm{R}}^{-1/2}$ with $V \to U$ and $L \to a$ — and identifies the wavenumber for stationary waves, $(\beta/U)^{1/2}$, which is the reciprocal of the Rhines length discussed below.

Armi (1989) develops the Froude-number analogy for hydraulic control of an eastward current with half-width a interacting with Rossby waves. Armi (1989) cites Fultz (1961) for $\mathrm{Ro}_\beta = U/\beta a^2$, who cites Long (1952). More recently, Y. Afanasyev et al. (2008) present an experimental study of cylinder wakes on a β-plane using the altimetric imaging velocimetry technique employed in this article.

2.2.2 M_R and the turbulence-to-waves transition

In general, there is nothing intrinsic to a rotating fluid that requires the PV gradient to be dominated by its meridional component. Except, when jets are just beginning to form, the relative vorticity gradient is weak and the planetary β does provide a meridional bias to the full PV gradient, which translates into a zonal bias for wave propagation and jet formation. The same holds true for a rotating tank with meridionally varying, zonally symmetric bottom topography, and for the troposphere of a gas giant that has abyssal zonal jets setting its lower boundary condition. Vallis and Maltrud (1993) demonstrate of how this zonal bias for emerging jets evolves in wavenumber space.

Rhines (1975) equates the frequency of Rossby waves to the rotational frequency of eddies to obtain a length-scale separating the domain of smaller eddies, which are isotropic, from larger ones, which have wave-like zonal bias. This leads to the squared Rhines length,

$$L_\mathrm{Rh}^2 = \frac{u}{\beta}\,. \tag{18}$$

An analytical advantage of (18) is that β is a constant on a β-plane, such that if u is also a representative constant, then the analysis is simplified because L_Rh^2 becomes an external parameter. However, as already noted, the fluid itself cannot pick β out of β_e, and the circulations on Jupiter and Saturn have $\beta_e/\beta = \pm 3$ (Ingersoll et al., 1981; Dowling & Ingersoll, 1989; Read et al., 2006; Read, Conrath, et al., 2009; Li et al., 2021). In light of this, one should employ the complete PV gradient and upgrade L_Rh^2 to be

$$L_\mathrm{jet}^2 = \frac{u}{\beta_e}\,. \tag{19}$$

(Although L_jet^2 is squared, it should be kept in mind that it can easily be negative.) The dimensionless variable M_R^{-1} now comes into play, because in the longwave limit, $\kappa^{-2} \to L_\mathrm{d}^2$ and the zonally symmetric version of (17) with (19) yields

$$M_\mathrm{R}^{-1} = \kappa^{-2}\frac{\beta_e}{u} \to \left(\frac{L_\mathrm{d}}{L_\mathrm{jet}}\right)^2\,. \tag{20}$$

This reveals that M_R^{-1} is a type of jet Burger number (albeit one that can easily be negative). It follows from (20) that $(L_\mathrm{d}/L_\mathrm{jet})^2 < 1$ implies shear stability ($M_\mathrm{R}^{-1} < 1$) and that $L_\mathrm{jet} = L_\mathrm{d}$ corresponds to the "sonic" or choked PV case ($M_\mathrm{R}^{-1} = 1$).

In this study, jets form via a turbulence-to-waves process called the β-plume mechanism. A β-plume is a flow structure that grows horizontally from spatially localized forcing in the presence of a background PV gradient. It is essentially a gyre consisting of two zonal jets flowing in opposite directions. The linear theory of Rossby waves emitted by a localized perturbation provides a straightforward explanation for the creation of β-plumes. Studies using the Green's function approach show that when the local forcing is switched on, it emits a spectrum of Rossby waves from which high-frequency transients propagate away, leaving behind low-frequency waves that have nearly zonal wave-crests (Stommel, 1982; Davey & Killworth, 1989; Y. D. Afanasyev & Ivanov, 2019).

2.2.3 M_R and shear stability

In 1880, the year that shear-stability theory began in earnest with Rayleigh's inflection-point theorem, Kelvin makes a major contribution as well by arguing on energetic grounds

that for inviscid vortical systems there are two branches of stability (Thomson, 1880). Geometrically, Kelvin's point is that the closed contours on a topo map, which he envisions to be the appropriate energy field associated with a stable configuration, can either be associated with a depression or a hill. Arnol'd (1966) establishes these two branches rigorously by constructing the relevant topo map out of a combination of perturbation energy and squared perturbation vorticity (enstrophy). Today this is called the pseudoenergy, and these two branches are called the Kelvin-Arnol'd-I and Kelvin-Arnol'd-II (KA-I and KA-II) stability branches.

McIntyre and Shepherd (1987) apply both branches to geophysical flows and show that they take the form $\partial\psi/\partial q > 0$ and $\partial\psi/\partial q < -\kappa^{-2}$, respectively, where κ^2 is the gravest eigenvalue relating the eddy PV to the eddy streamfunction, $q' = -\kappa^2\psi'$, and is the same as in (16). Non-dimensionalizing these is straightforward and insightful (Dowling, 2014): given (17), the dimensionless versions of KA-I and KA-II are $M_\mathrm{R} < 0$ and $M_\mathrm{R} > 1$, respectively . It is thus evident that KA-I and KA-II refer to the two "supersonic" cases, and that these concatenate into one compact statement in terms of the reciprocal,

$$\text{stable}: \quad M_\mathrm{R}^{-1} < 1\,. \tag{21}$$

The physical intuition associated with KA-I and KA-II boils down to this: "supersonic" critical latitudes are stable.

3 Experimental set-up and data acquisition

The experiments are performed in a cylindrical tank of radius $R = 55\,\mathrm{cm}$ that is installed on a rotating table (Figure 1a). The tank is filled with water of mean depth $h_0 = 14\,\mathrm{cm}$ and then rotated counterclockwise with angular velocity $\Omega = 2.4\,\mathrm{rad\,s^{-1}}$.

3.1 Bottom topography with two critical latitudes

The key feature is the tank's bottom topography, $\eta_b(r)$, which varies with respect to radius in a triangular or tent-shaped fashion that is azimuthally symmetric (Figure 1b). The peak height of the bottom topography is 8 cm and the base of the triangle is 30 cm wide. As a result of this combination of surface and bottom topographies, the tank naturally partitions into four zones (Figure 2a): Zone 1 ($0 < r < 20\,\mathrm{cm}$) is a polar area where depth increases modestly with radius; Zone 2 ($20 < r < 35\,\mathrm{cm}$) has depth decreasing sharply due to bottom topography; Zone 3 ($35 < r < 50\,\mathrm{cm}$) has depth increasing sharply; and Zone 4 ($50 < r < 55\,\mathrm{cm}$) is an equatorial annulus where depth increases less sharply.

The discussion above concerning the PV gradient in Cartesian geometry carries over to a cylindrical tank, with $f = f_0 = 2\Omega$, $\beta = df/dy = 0$, $dr = -dy$. The cylindrical-coordinate map factors are accounted for in the calculation of relative vorticity,

$$\zeta = \frac{1}{r}\frac{\partial(ur)}{\partial r} + \frac{1}{r}\frac{\partial v}{\partial\theta}\,, \tag{22}$$

where θ is the azimuthal angle, positive in the counterclockwise (prograde, eastward) direction, $u = rd\theta/dt$, and $v = -dr/dt$. In the undisturbed case, $\zeta = 0$ and $\beta_u = 0$, and consequently the PV gradient, β_e, is due to the undisturbed β_h term alone, which by (4) is $\beta_h = -fh_y/h = 2\Omega h_r/h$. Since h is given by the difference between the parabolic surface, η_geoid in (5), and the tent-shaped bottom topography, η_b in Figure 2a, the PV gradient is (Figure 2b)

$$\beta_h(r) = \frac{2\Omega}{h}\left(\frac{\Omega^2}{g}r - \frac{d\eta_b}{dr}\right)\,. \tag{23}$$

This configuration initializes the tank with one strong critical latitude (in terms of the jump in β_h) positioned over the peak of the ridge, and one weak one positioned over the

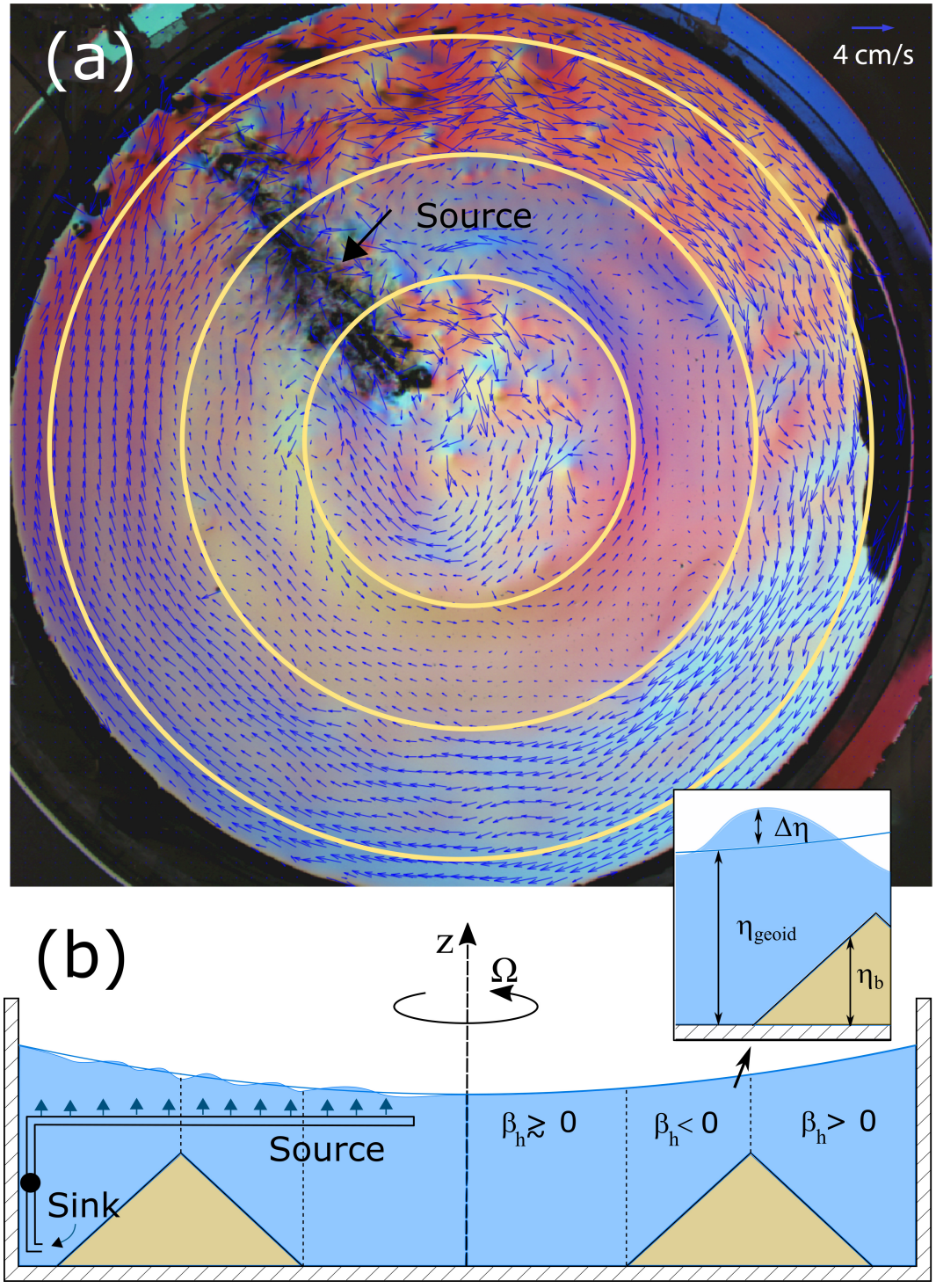

Figure 1. Experimental set-up: (a) top view of the tank as seen by the nadir-pointing video camera with superposed velocity vectors and (b) cross-section of the tank. Yellow circles in (a) correspond to the radial positions of the outer edge, peak, and inner (polar) edge of the tent-shaped bottom topography. The sign of topographic β_h is indicated in (b) for each region; it is negative between the peak and inner edge of the triangular bottom, which sets up two critical latitudes (radial positions) where β_h changes sign.

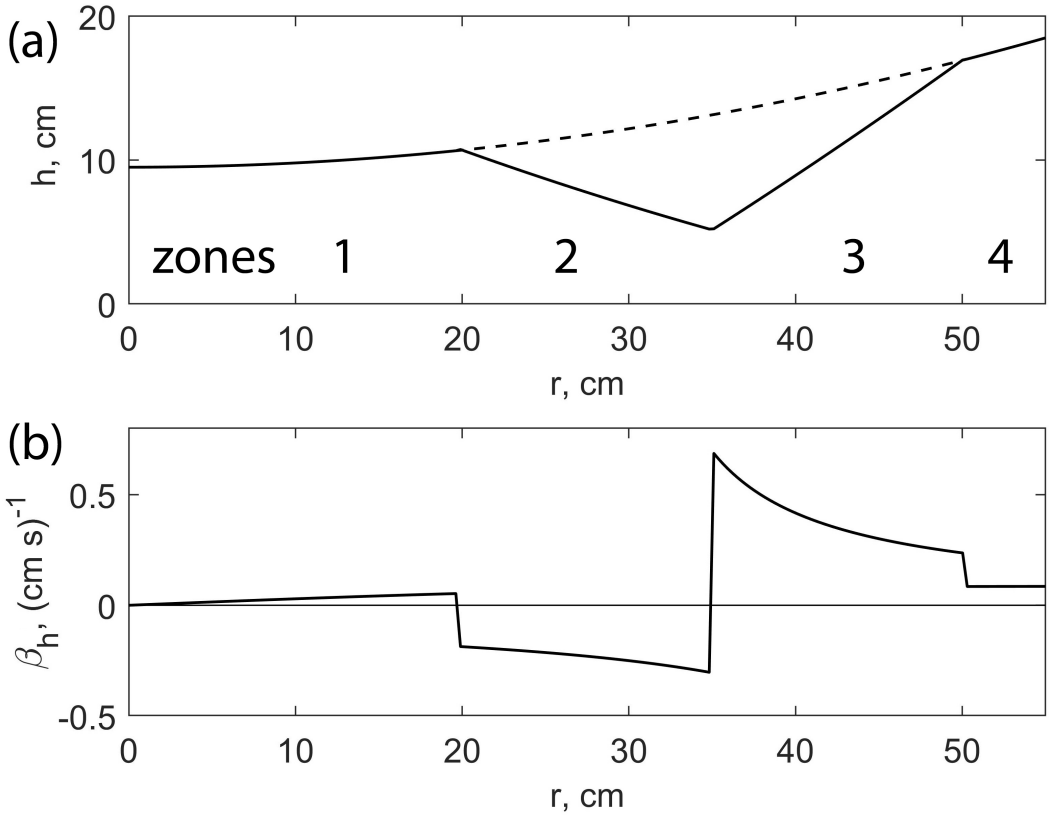

Figure 2. Profiles for rotating, unforced tank versus radius, r: (a) water depth and (b) topographic β_h. Dashed line in (a) is unforced geoid height, η_{geoid}. By design, there are two topographic critical latitudes where β_h changes sign, located on the boundaries of Zone 2.

poleward foot of the ridge (at the boundary with Zone 1). Inside of Zone 2 the PV gradient is negative, and outside it is positive, weakly so in Zone 1 (the polar region) and more strongly so in Zones 3 and 4.

3.2 Forcing

Flow in the tank is forced by a fresh-water source-and-sink combination driven by a pump, with fresh water throughout the tank. In its details this approach is new, but it is similar to the forcing used by Y. D. Afanasyev et al. (2012), in which a linear source of fresh/buoyant water is injected into a tank of salt water, without a sink. In this study, there is a sink at the bottom of the tank near the wall, and the source is a radial pipe with multiple small holes drilled along its entire length, as shown in Figure 1b, which is connected to the sink via a remote-controlled pump. The pipe is under the surface of the water and extends from the wall to the center of the tank. The holes in the pipe face upwards and create strong vertical jets and intense turbulence above the pipe. Pumping intensity is an external control parameter, which is held constant during each experimental run and varied between them. This pumping sets up a tank-sized anticyclone, and consequently a convenient non-dimensional measure of the forcing strength is the difference between $\Delta\eta = \eta - \eta_{\text{geoid}}$ at the center of the tank and that at the outer wall (azimuthally averaged), divided by the average depth, h_0:

$$\delta_f = \frac{\Delta\eta(0) - \overline{\Delta\eta}(R)}{h_0} \,. \tag{24}$$

This forcing parameter δ_f is calculated during the statistically steady period in each experiment.

Run	δ_f [%]	Transient Rotations	Statistically Steady Rotations
1	0.9	0–25	25–150
2	1.9	0–35	35–230
3	2.5	0–35	35– 90

Table 1. Summary of control parameters for the experimental runs. The strength of forcing is quantified by δ_f as defined in (24).

Three full-length runs are recorded, with the forcing summarized in Table 1. Qualitatively similar results are obtained in all three experiments, so most of the following analysis focuses on Run 2, which is the longest one. Run 1 serves primarily as an initial practice run; apart from successfully testing the forcing and data acquisition systems, and demonstrating that forcing stronger than $\delta_f = 0.9\%$ should be tried, it is not mentioned further. Run 3 has about 30% stronger forcing than Run 2 and is used to verify that the features seen in Run 2 are robust. The statistically steady period for each run, the period after the zonal jets have encircled the tank, is estimated by inspection of space-time (Hovmöller) diagrams; for example, for Run 2 it begins around $t = 35$ rotations (see Figure 4).

3.3 Altimetric Imaging Velocimetry (AIV)

The two horizontal components of the gradient of $\Delta\eta$ are measured using the Altimetric Imaging Velocimetry (AIV) technique. See Y. D. Afanasyev et al. (2009) for details on the local-water-surface versus lab coordinates associated with this technique. The gradient is obtained by processing a video sequence of each experiment frame by frame.

The videos are recorded by a nadir-pointing, co-rotating camera installed above the tank. Horizontal velocity is estimated to first order in Rossby number, $\mathrm{Ro} = |\zeta|/\mathrm{f}_0$, via geostrophic balance and improved to second order (e.g. Cushman-Roisin et al., 1990) via

$$\vec{v} = \frac{g}{f_0}\hat{k} \times \vec{\nabla}(\Delta\eta) - \frac{g}{f_0^2}\vec{\nabla}(\Delta\eta_t) - \frac{g^2}{f_0^3} J\left(\Delta\eta, \vec{\nabla}(\Delta\eta)\right) . \tag{25}$$

The first term on the right-hand side is geostrophic balance (6). In the second term, the temporal derivative or tendency, $\Delta\eta_t$, is calculated via finite difference between two successive frames in the video sequence, with a time interval of approximately 0.15 s. In the third term, J is the Jacobian operator (the determinant of the matrix of partial derivatives), which in Cartesian geometry is $J(A, B) = A_x B_y - B_x A_y$. The Rossby number satisfies $\mathrm{Ro} \lesssim 0.2$ everywhere in the flow, except in the vicinity of the source pipe (where it exceeds unity), hence away from the forcing (25) is accurate to 4% (i.e. $\mathrm{Ro}^2 \lesssim 0.04$).

4 Results

Laboratory experiments allow for detailed observations of the evolution in time of the developing jets and shear flows, which are difficult or impossible to obtain for planetary systems but can provide insights into how statistically steady patterns emerge.

4.1 Eddies, waves, and plumes

Analyses of the video sequences reveal the emergence and evolution of a variety of eddies, waves, and plumes. Figure 3 shows snapshots of the flow taken at the beginning of Run 2, during a period spanning 16 rotations. Multiple small-scale vortical eddies are created by the thin jets injected from the pipe, and several different types of waves develop.

4.1.1 Gravity waves

Turning on the forcing generates surface gravity waves (buoyancy waves) that are fast and have high frequency such that they are almost unaffected by rotation. Their phase propagates away from the forcing in the familiar sense of a rock thrown into a pond. When these waves are slow enough to feel the Coriolis acceleration, but with frequency still greater than 2Ω, they are called inertia-gravity waves. These waves don't contribute significantly to the overall dynamics and can be filtered out during data processing if desired. The forcing also generates transient Kelvin waves, which are half waves or shelf waves that exist when there is a support on their right-hand side that they can lean against. These can be seen propagating quickly eastward (prograde, counterclockwise) along the wall of the tank (Figure 3a). Their speed is equal to the fast speed of long gravity waves, $c = (gh)^{1/2} \approx 120\,\mathrm{cm\,s^{-1}}$, such that they travel around the tank in less than 3 s, faster than one period of rotation. Kelvin waves are only observed briefly after the initial transient of turning on the forcing.

4.1.2 Inertial waves

Distinct from inertia-gravity waves, thin stripes of inertial waves, also known as gyroscopic waves, can be seen in Figure 3. Inertial waves have frequency less than 2Ω and are an important component of the dynamics of oceans and planetary atmospheres (Kelvin, 1880; Maas, 2001; Rabitti & Maas, 2013). They can be identified in a flow due to the peculiar property that their phase propagates towards the source of the perturbation, rather than away from it. Thus, when inertial waves are generated by an eddy, the concentric pattern of the waves looks like it is collapsing into the eddy. These waves are omnipresent in the tank, particularly near the forcing area.

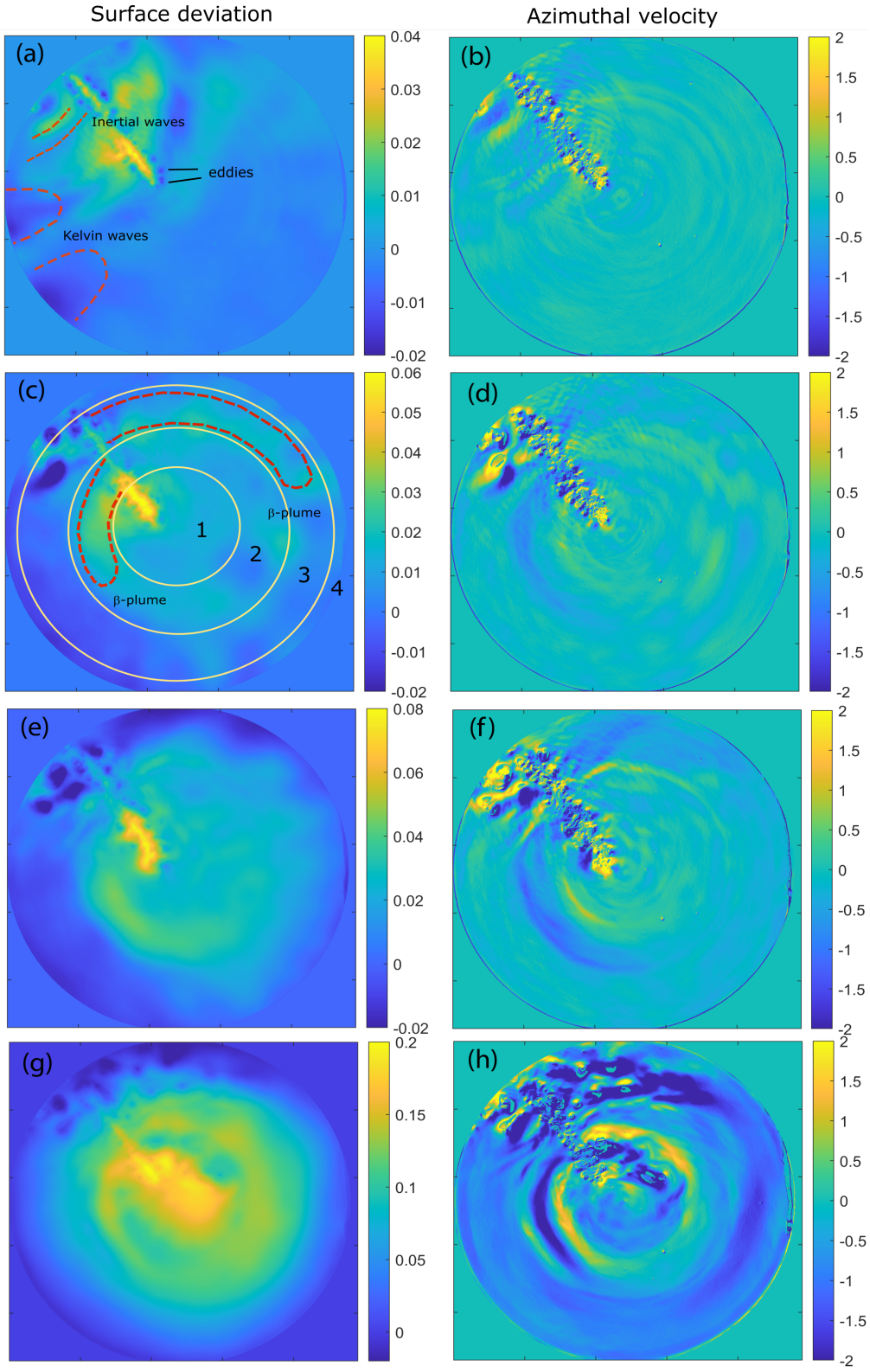

Figure 3. Initial evolution of rotating and forced flow (Run 2). Surface deviation, $\Delta\eta$, in cm (left column) and zonal (azimuthal) velocity, u, in cm/s (right column), for $t = 0.9$ (a, b), 1.8 (c, d), 3.0 (e, f) and 16.0 (g, h) rotations. Inertial waves, Kelvin waves, and eddies are labeled in (a). The four zones of bottom topography are numbered as in Figure 2 and indicated with yellow circles in (c). A westward (retrograde) β-plume emanates from the forcing in the positive-β_h Zone 3, whereas an eastward (prograde) β-plume emanates from the forcing in the negative-β_h Zone 2.

4.1.3 Rossby waves and β-plumes

Arguably the most important waves for the evolution of jets and large-scale circulations are Rossby waves. As discussed in Section 2.1.4, Rossby waves oscillate in order to conserve PV in the presence of an environmental PV gradient. The nature of this restoring force has at least two important ramifications for the evolution of jets. Firstly, these waves affect jet dynamics wherever vorticity gradients are present, and jets by their nature associate with vorticity and shear—a more generic name for Rossby waves would be vorticity waves. Secondly, Rossby waves are planetary in scale and are sensitive to bottom and surface slopes. Hence they are diagnostic of the boundary conditions that lie beneath a system's visible jets, like the dynamic topography associated with Jupiter's abyssal jets, or the bottom topography in this study.

Rossby waves exhibit a difference in character depending on whether they are longwave or shortwave. Recall from (15) that Bu is the dimensionless horizontal wavenumber. Significantly, in the longwave limit, $\mathrm{Bu} \to 0$, Rossby waves are non-dispersive such that their zonal phase speed (ω/k) and group velocity ($\partial\omega/\partial k$, i.e. their envelope velocity) asymptote to the same fastest value relative to the flow, $\hat{c} = -\beta_e L_d^2$. In regions where $\beta_e > 0$, such as Zones 1, 3, and 4 (Figure 2), this is westward (retrograde, clockwise) of the forcing. But in regions where $\beta_e < 0$, such as Zone 2, this is eastward (prograde, counterclockwise).

In suitably forced systems, Rossby waves manifest as β-plumes (Stommel, 1982; Davey & Killworth, 1989; Y. D. Afanasyev & Ivanov, 2019). For short-enough wavelengths, the intrinsic group velocity switches direction (Vallis, 2017), and in the tank long zonal jets and non-linear transport are observed to set up on the longwave side of the forcing, and short, wavy patterns are observed to set up on the short-wave side. Two distinct β-plumes are evident in Figure 3, highlighted with red-dashed outlines in panel c. The plume in Zone 3, where $\beta_e > 0$, expands primarily westward, which is expected since this is its longwave group direction. This plume's overall surface-deviation is negative, $\Delta\eta < 0$, and so it is a low-pressure anomaly with cyclonic circulation. Contrast this with the Zone-2 plume, where $\beta_e < 0$, which expands primarily eastward, which is its longwave group direction. It is intriguing to watch the two plumes evolve in opposite directions next to each other, reminiscent of the alternating jets on Jupiter and Saturn. The Zone-2 plume has $\Delta\eta > 0$ and so is a high-pressure anomaly with anticyclonic circulation (Figure 3d,f,h). In the polar region where $\beta_e \approx 0$ (Zone 1), there are no discernible β-plumes, but instead a growing collection of vortical eddies.

4.2 Hovmöller diagrams

A useful way to visualize the development of the flow is to pick a particular radius and plot a space-time diagram, called a Hovmöller diagram, with time running horizontally and longitude (azimuthal angle) running vertically. The separate panels in Figure 4 show the evolution of the zonal (azimuthal) velocity at four different radii: in the middle of the polar region (Zone 1), at the boundary between the polar and negative β_e regions (between Zones 1 and 2), and in the middle of the negative and positive β_e regions (in Zones 2 and 3). The azimuthal angle, θ, is measured counterclockwise from the source, which can be easily identified by its small-scale perturbations, and is plotted down the page. For orientation, one can consider the view to be overhead, with the center of the tank on the right and the source located between $\theta = 360°$ and $0°$. In these diagrams, retrograde and prograde drifts correspond to coherent markings oriented in the right-leaning and left-leaning (/ and \ ) senses, respectively. The zonal velocity itself can be negative or positive, which is shown in blue or yellow, ranging from -2 to $2\,\mathrm{cm\,s^{-1}}$. Slower or faster zonal drifts correspond to more horizontal or more vertical slopes. The nearly vertical, fine-scale eddies are fast gravity waves that are continuously emitted by the source and reflected from the walls of the tank.

4.2.1 Zone 1

Consider first Zone 1, the polar region, shown in Figure 4a. Relatively large eddies are created on the westward (retrograde) side of the source ($\theta = 360°$) and are advected by the local retrograde (/) circulation. Rossby waves propagating in the westward sense are weakly present, since β_e is weakly positive in Zone 1. For the large eddies there is a noticeable change in character from irregular to smooth bands about halfway around the tank, implying that the waves are transforming into smooth β-plumes.

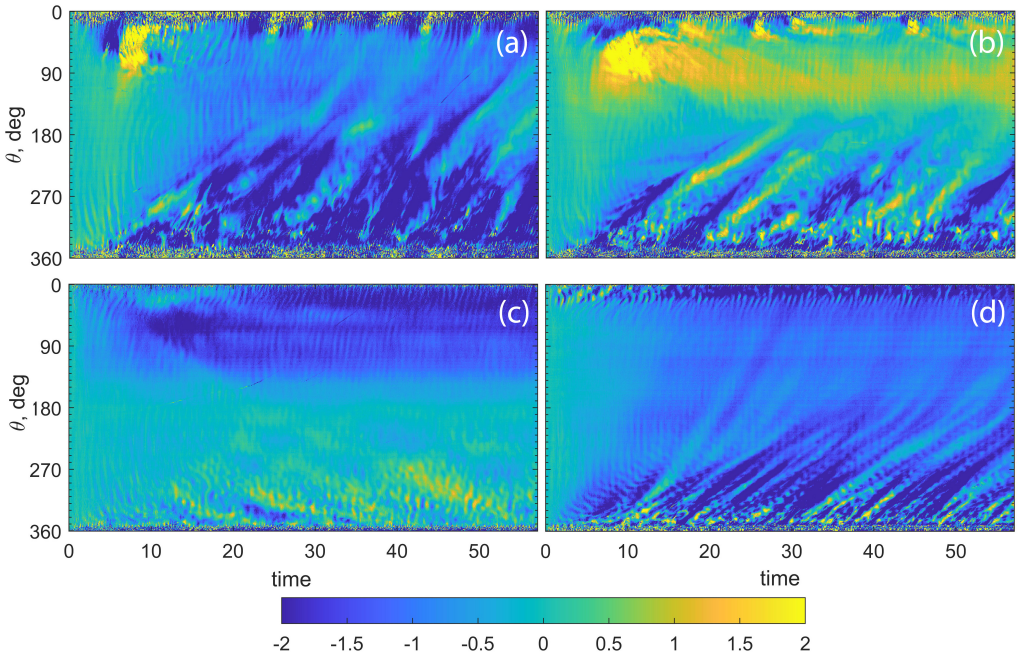

Figure 4. Hovmöller (space-time) diagrams (Run 2) of zonal (azimuthal) velocity, $u = rd\theta/dt$, measured along the concentric circles of radius $r = 15$ cm (a); 20 cm (b); 28 cm (c); and 40 cm (d). These positions are within the polar region (Zone 1), at the boundary between the polar and negative β_h regions (between Zones 1 and 2), in the middle of the negative β_h region (Zone 2), and in the middle of the positive β_h region (Zone 3); compare with Figure 2. Time is in units of rotation period. The statistically steady interval begins at about rotation 35. Color scale is in cm/s.

4.2.2 Zone 2

Now consider the transition to the negative β_e region (the interface between Zones 1 and 2), shown in Figure 4b. This is in the vicinity of the system's weaker critical latitude. The bottom half of the panel (180° to 360°) is similar to Zone 1, with retrograde drift of large eddies. However, the top half (0° to 180°) is different, with no large eddies but with a band of prograde (yellow) velocity that is the signature of the zonal jet at the poleward flank of the β-plume in Zone 2. In addition, small eddies emanate from the source and propagate in the prograde (\ ) direction. Rossby waves propagating eastward like this are observed on Jupiter where $\beta_e < 0$ (e.g., Rogers et al., 2016).

Moving into the middle of the negative β_e region (Zone 2), Figure 4c is positioned along the equatorward flank of the β-plume (see Figure 3c). A band of retrograde (blue) velocity extends from the source to approximately halfway around the tank ($\theta = 0°$ to

180°). Even though this position is in between two critical latitudes, namely the flanks of Zone 2, the flow in this area lacks major perturbations and is stable. Retrograde of the forcing (on the bottom half of the figure), overlying a mean speed that is approximately zero (green), there exists a crisscross pattern of small eddies with prograde and retrograde speeds. These are small-scale vortical eddies created by the pipe's jets.

4.2.3 Zone 3

Figure 4d is positioned past the strong critical latitude between Zones 2 and 3 and into the middle of the positive β_e region of Zone 3. Overall, the eddies are less vigorous and finer than in Zone 1, but there is a general resemblance, including the transition in the top half to smooth β-plumes. The dispersive nature of Rossby waves is nicely evident in this panel, with smaller wavenumber features propagating faster than larger wavenumber features (i.e., longer wavelengths are propagating faster).

A general result of the Hovmöller analysis is that the character of the flow differs between the prograde and retrograde halves of the tank relative to the diameter containing the mass source (i.e. the top and bottom halves of the diagrams). This asymmetry is a peculiarity of the forcing method being used, but is interesting in its own right and is explored next.

4.3 Monopolar and dipolar components

A variety of methods have been devised for forcing laboratory experiments, not to mention numerical simulations, and it is helpful to distinguish between the components of the reaction that are intrinsic to the system versus those that associate with the forcing method. In these experiments, the forcing is mass injection that is localized along a particular radius of the tank, rather than some type of more-or-less uniform distribution. A consequence is the introduction of an azimuthal dipolar component to the evolution, in addition to the anticipated β-plumes and zonal jets.

To separate out the dipolar component, a fast Fourier transform (FFT) of $\Delta\eta(r,\theta)$ with respect to θ is calculated at each radius. The zeroth and first-order amplitudes from the FFT then yield the monopolar and dipolar components, which may be written conveniently in terms of real factors as

$$\Delta\eta(r,\theta) = M(r) + a(r)\cos\theta + b(r)\sin\theta + \dots\,, \tag{26}$$

where the monopolar component, $M(r)$, is the zonal (azimuthal) average. An example decomposition is shown in Figure 5 for Run 2, after 3 rotations of the tank. The full $\Delta\eta$ is shown in Panel (a), with the axis of the dipole indicated by a dashed line, which nearly aligns with the forcing radius, as expected. The monopolar and dipolar components are isolated in Panels (c) and (d), respectively.

4.3.1 Monopolar component

Consider first the monopolar component, $M(r)$, in Figure 5c. The mass injection generates a tank-sized anticyclonic vortex, except at the tank's center, where the source-pipe does not reach and the flow develops cyclonic circulation, and at the tank's periphery, where the mass sink is located. The sink is a drain-pipe with a relatively wide ($\sim$ 1 cm diameter) opening, located at the bottom near the wall, about 10 cm counterclockwise from the source-pipe. The sink does not strongly affect the momentum of the tank, although it does create small cyclones that can be seen in the images; these generate a low-pressure β-plume that propagates along the wall in Zone 4. These various patterns can be seen in the velocity vectors shown in Panel (c). Within this general circulation, alternating zonal jets form via the β-plume mechanism, with their direction controlled by the sign of β_e.

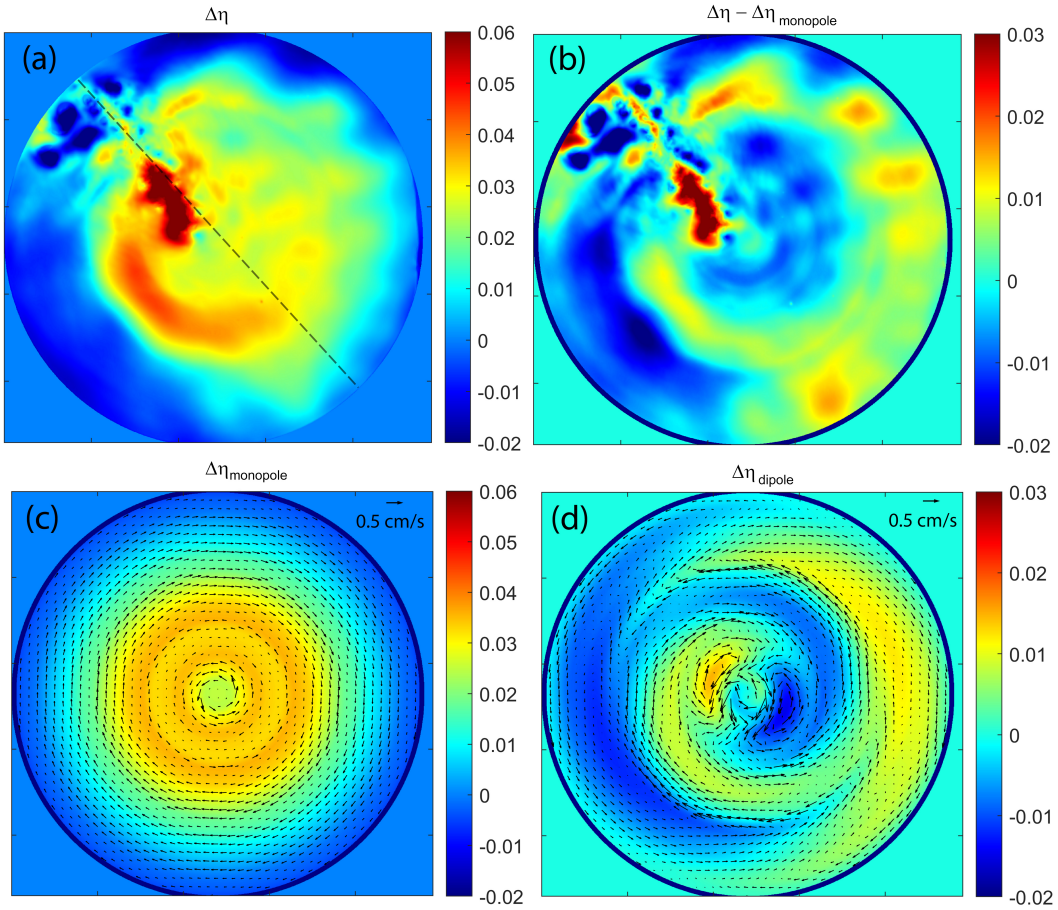

Figure 5. Monopolar and dipolar components of the flow (Run 2): (a) original surface deviation field at $t = 3$ rotations of the tank, (b) the residual of the field when the monopolar component is subtracted, (c) the monopolar component and (d) the dipolar component obtained by the decomposition (26). Dashed line in (a) shows the axis of the dipole. Surface deviation is in cm; arrows in (c) and (d) show respectively the monopolar and dipolar velocity fields.

4.3.2 Dipolar component

The dipolar component (Figure 5d) is only two times smaller in magnitude than the monopolar component. Figure 5b shows the residual field with the monopolar component subtracted, $\Delta\eta - \Delta\eta_{\text{monopole}}$. The dipolar component is evident, as are higher-order angular modes. The axis of symmetry aligns with the source. Such dipolar structures, with analogies to features seen in Earth's polar regions, have been previously studied in similar experimental set-ups and are relatively well understood. For example, Y. D. Afanasyev and Jewtoukoff (2009) use the same laboratory altimetry technique employed here to study dipoles that are generated by a force centered at the pole, rather than via an off-center mass source/sink.

4.4 Statistically steady circulations

Once β-plumes encircle the tank, a mature circulation is reached that includes complete alternating zonal jets, as well as embedded jet streaks that are provoked by the continuous forcing. Figure 6 shows surface deviation, velocity, and vorticity from the dynamically steady state period of Run 2, at $t = 51$ rotations. Consider first the large-scale pattern of the flow revealed by $\Delta\eta$, shown in Panel (a). The anticyclonic circulation is evident: $\Delta\eta$ is high in the tank center and generally decreases to the wall. In addition, an annulus of positive $\Delta\eta$ at $r \approx R/2$ is evident, which corresponds to the β-plume in Zone 2.

4.4.1 Velocity and vorticity fields

Next consider medium and small scales revealed in the zonal velocity, u, shown in Panel (b). Bands of different color in u indicate both complete zonal jets and jet streaks within the general anticyclonic circulation. In the outer, positive-β_e region (Zones 3 and 4) there are cyclonic jet streaks (green and yellow) that are opposing the large-scale anticyclonic circulation (blue) but are not strong enough to prevail. Zone 2 has anticyclonic flow, but in addition there is a distinct cyclonic (yellow) jet sitting on the border with Zone 1 that persists throughout the mature phase of the run.

Medium and small-scale features are also evident in the PV shown in Panel (c). In Zone 1, cyclonic and anticyclonic eddies are co-mingling, which tends to homogenize PV. The two built-in critical latitudes in the interior of the system are visible: the stronger one is the pronounced green-yellow-green (maximum q) annulus situated over the ridge of the bottom topography, and the weaker one is the more subtle green-blue-green (minimum q) pattern on the border between Zones 2 and 1. These are analyzed below.

4.4.2 M_{R}^{-1} and Rossby waves

As reviewed above, the reciprocal of the analog of the Mach number for Rossby waves, M_{R}^{-1} (Figure 6d), has emerged as a useful diagnostic for systems with evolving jets. One advantage of the reciprocal over M_{R} itself is that it concatenates the Kelvin-Arnol'd I branch (KA-I) of shear stability theory, $M_{\text{R}} < 0$, and the Kelvin-Arnol'd II branch (KA-II), $M_{\text{R}} > 1$, into one compact "supersonic" condition, $M_{\text{R}}^{-1} < 1$. As a consequence, two important but distinct PV concepts, PV mixing and shear stability, are non-dimensionalized and clarified via M_{R}^{-1} into a discussion of "0 versus 1" (Dowling, 2020).

On the large scale, the most striking feature of Figure 6d is its bulls-eye pattern: proceeding from out to in, Zones 4 and 3 are mostly blue, Zone 2 is mostly white, and Zone 1 is mostly green. Consider first Zones 4 and 3. The KA-I branch corresponds to negative M_{R}^{-1} or M_{R}, which is rendered blue in Figure 6d. This branch is logically equivalent to the Fjørtoft and Ripa shear-stability criteria. By making judicious choices of the Galilean shift in $(\overline{u} - \alpha)$, KA-I also includes as special cases the Rayleigh, Kuo and

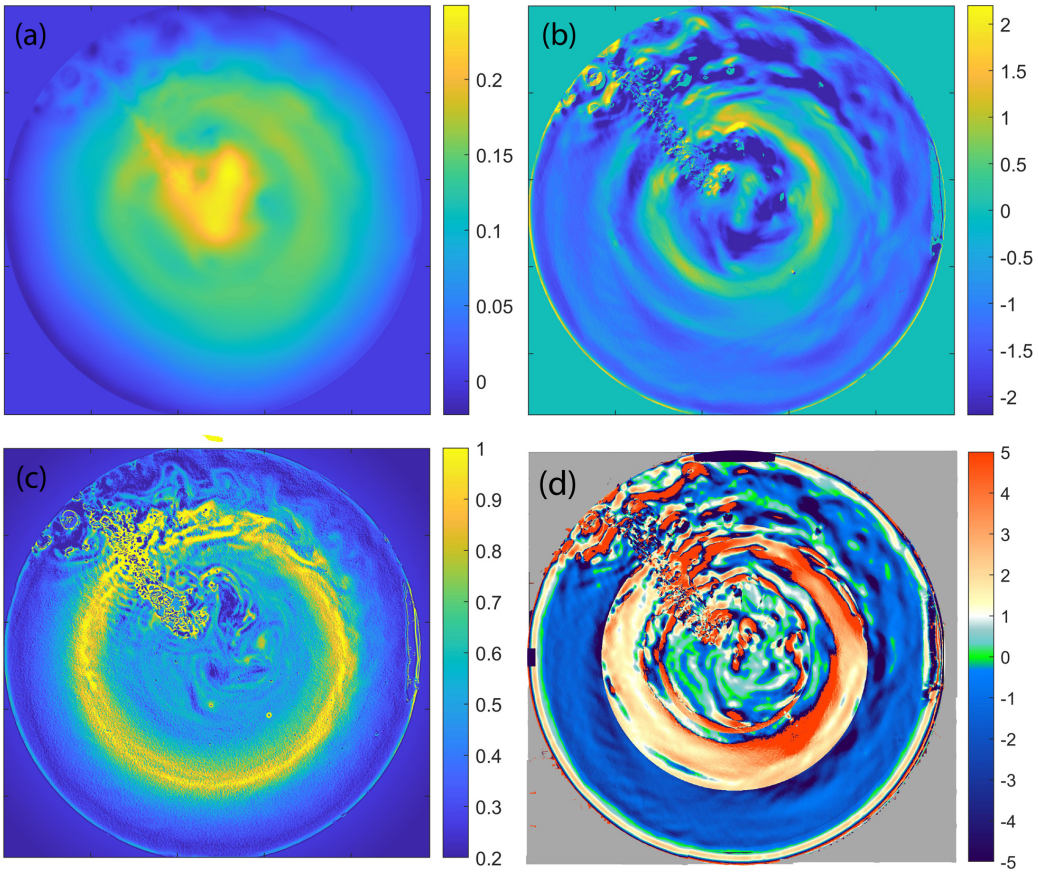

Figure 6. Features of mature circulation (Run 2, $t = 51$ rotations). Shown are (a) surface deviation, $\Delta\eta$, in cm, (b) zonal velocity, u, in cm/s, (c) potential vorticity, q, in $(\text{cm s})^{-1}$ and (d) reciprocal "Mach" number, M_{R}^{-1}, calculated in the tank's rotating reference frame. A special color scale is used in (d) to highlight where M_{R}^{-1} is near zero versus near unity (green or white), which corresponds to homogeneous/mixed PV versus choked/"sonic" PV, respectively.

Charney-Stern stability criteria (see Dowling, 2019, and references therein). Zones 4 and 3 are evidently KA-I stable, except near the source. This is reasonable, since the general circulation in these two zones is anticyclonic (westward), and since $\beta_e > 0$, Rossby waves propagate westward (15), which is downstream (blue). Notice that whether or not there are critical latitudes in Zones 4 and 3 does not come up—the dog does not bark—since they are only relevant to instability in red regions. In other words, blue and green ("supersonic") critical lines are innocuous, as in practice are white ones ("sonic"). There are red patches near the source region in Zones 4 and 3 that are quite turbulent.

Zone 2 stands out as a mostly white annulus ("sonic" or choked PV) with some red. It also exhibits an intriguing annular feature on the border with Zone 1 that is blue, which corresponds to the yellow (eastward) jet in Panel (b). The green of Zone 1 indicates that all three components of β_e are small: β is zero across the tank, β_h is naturally small in the polar region (Figure 2), and the relative vorticity is not strong enough for β_u to make a significant contribution. The co-mingling vortices in Zone 1 originate mainly from the source pipe rather than from shear instability. On the whole, in Zone 1 the appropriate dimensionless version of β_e, namely M_{R}^{-1}, has little chance of being anything but ~ 0.

4.4.3 Numerator and denominator of M_{R}^{-1}

The focus now turns to the dynamics in the vicinity of the system's two built-in topographic critical latitudes. It is instructive to pull apart M_{R}^{-1} and simultaneously track the evolution of its numerator and denominator, $-\hat{c}_x$ and u, as a function of radius and time. To benefit from zonal averaging, but at the same time to avoid the complications around the source region, these variables are averaged over a sector of θ values. To average out small eddies and emphasize long Rossby waves, sectors of $\Delta\theta = 30^\circ$ to 45° (1.0 to 1.5 hours on a 12-hour dial) prove to be sufficient. As can be anticipated from the full-tank images, after the circulation is mature, any sectors that avoid the source pipe yield similar results. Sectors in the vicinity of 8 o'clock (where the top of the tank images is 12 o'clock, and the source pipe is at 10:40 o'clock) are displayed in what follows because this neighborhood is somewhat less affected by the perturbations advected from the forcing radius.

Figure 7a shows $-\hat{c}_x(r)$ and $u(r)$ separately during the entire Run 2. The zonal velocity profiles (blue) start with near-zero values but rapidly develop a quasi-steady pattern with a few distinct jets. The profiles collapse around this steady-state profile and vary only slightly afterwards, except in Zone 1 (the leftmost one) where the variability is significant at all times. Compare this with the (negative) intrinsic phase velocity profiles, $-\hat{c}_x$ (yellow). These start along the profile of β_h (red curve; use this to distinguish Zones 1 to 4 from left to right), but then evolve into a pattern generally following that of u, particularly in Zone 2. The only region where this $M_{\mathrm{R}}^{-1} \to 1$ process does not gain any traction is Zone 3. Figure 7b shows the same quantities averaged over short periods of time, using different line styles to indicate the temporal evolution. Variability of $-\hat{c}_x$ and u can be judged visually by the thickness of the yellow or blue profiles in Panel (a). To quantify this variability, we compute the standard deviation, σ, of both quantities during the steady-state period of Run 2 (Figure 7c). As expected, in Zone 1 the variability of both is significant. It decreases to a relatively small constant value in Zone 2. Intriguingly, $\sigma(-\hat{c}_x)$ and $\sigma(u)$ have robust peaks on both sides of critical latitude at $r = 35$ cm, with a minimum in between.

To test the effects of the strength of forcing, δ_f, snapshots taken during the statistically steady period of Runs 2 and 3 ($\delta_f = 1.9$ and 2.5%) are shown in Figure 8. These are averaged over the sector 7 to 8 o'clock ($\Delta\theta = 30^\circ$). In terms of $M_{\mathrm{R}}^{-1}(r)$, the runs are qualitatively similar across the tank. They are also similar in terms of $\overline{u}(r)$ in Zones 1 and 2, with somewhat stronger retrograde jets developing in Zones 3 and 4 for the stronger forcing case.

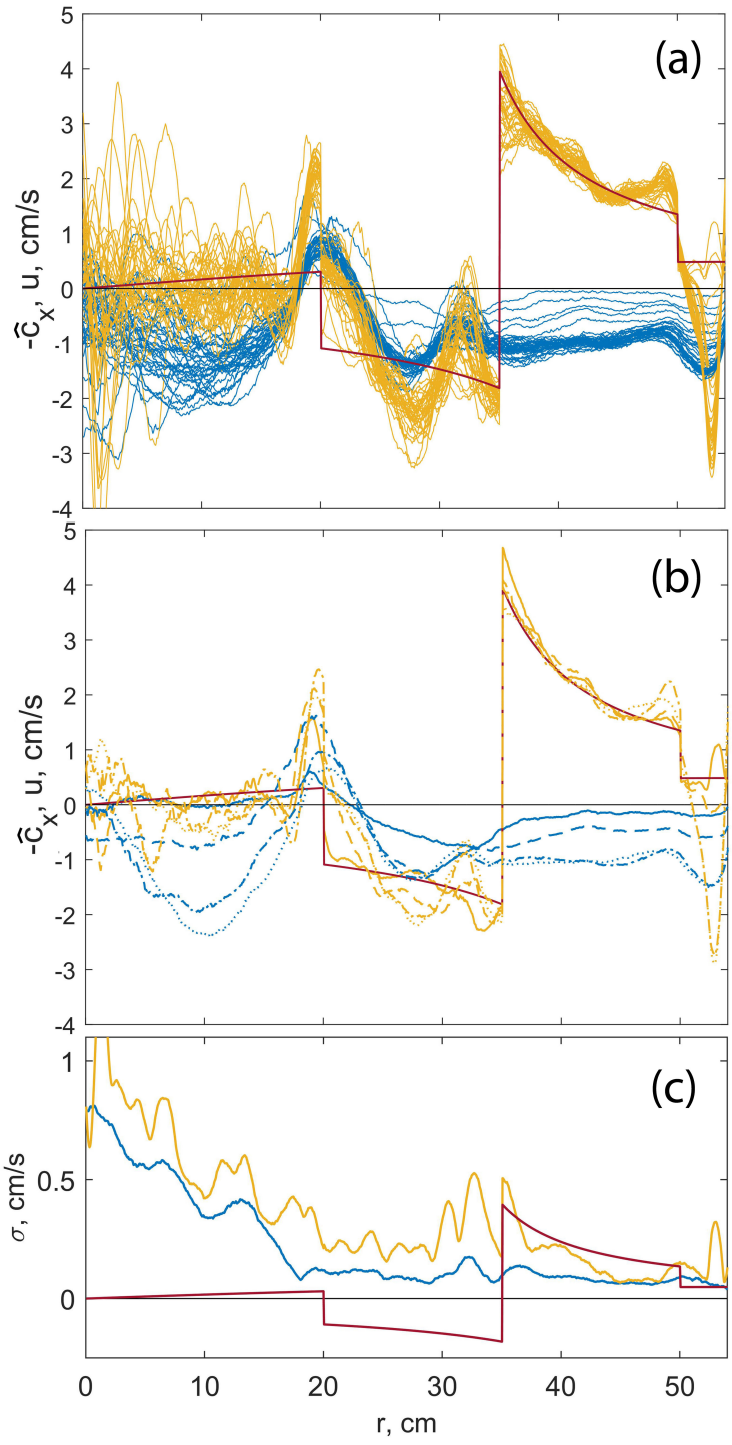

Figure 7. Radial profiles of the negative intrinsic zonal phase speed, $-\hat{c}_x(r)$, and the zonal velocity, $\overline{u}(r)$, in the sector between 6:30 and 8 o'clock (Run 2). Shown are (a) time sequences of $-\hat{c}_x$ (yellow) and u (blue), every 50 frames (2.9 rotations); (b) selected 5-rotation time averages of $-\hat{c}_x$ and u: t = 6–11 (solid lines), 12–17 (dashed lines), 55–60 (dash-dot lines) and 110–115 (dotted lines) and (c) standard deviation, σ, of $-\hat{c}_x$ (yellow) and u (blue) during the steady-state period. For reference, the red curve indicates $-\hat{c}_x$ based on undisturbed β_h; in panel (c) its magnitude is reduced by a factor of 10.

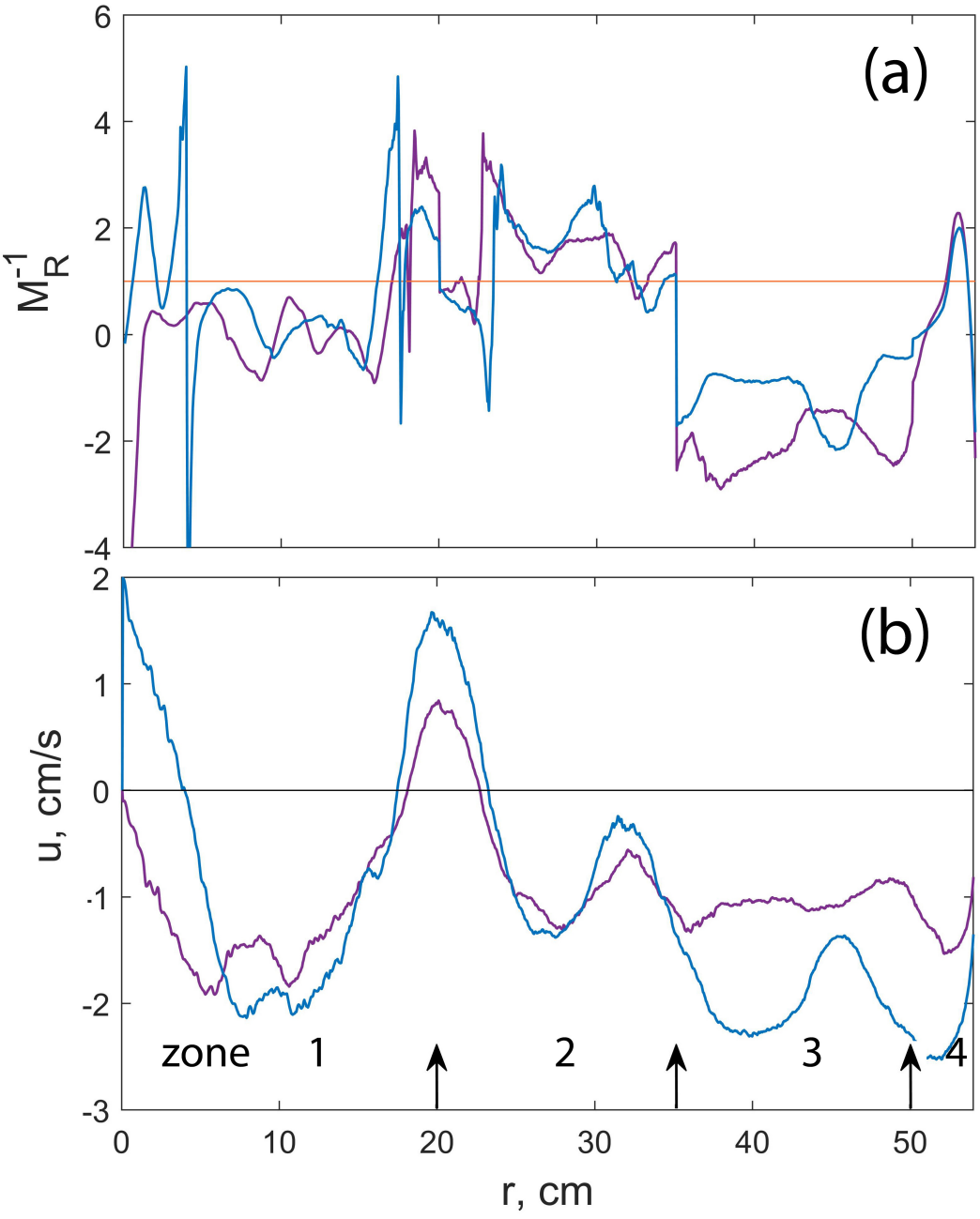

Figure 8. Radial profiles of (a) M_{R}^{-1} and (b) $\overline{u}$ averaged in the sector 7 to 8 o'clock, for weaker forcing (magenta, Run 2, $t = 51$ rotations, $\delta_f = 1.9\%$) and stronger forcing (blue, Run 3, $t = 57$ rotations, $\delta_f = 2.5\%$). Black arrows in (b) indicate the zone boundaries.

4.4.4 Galilean shift

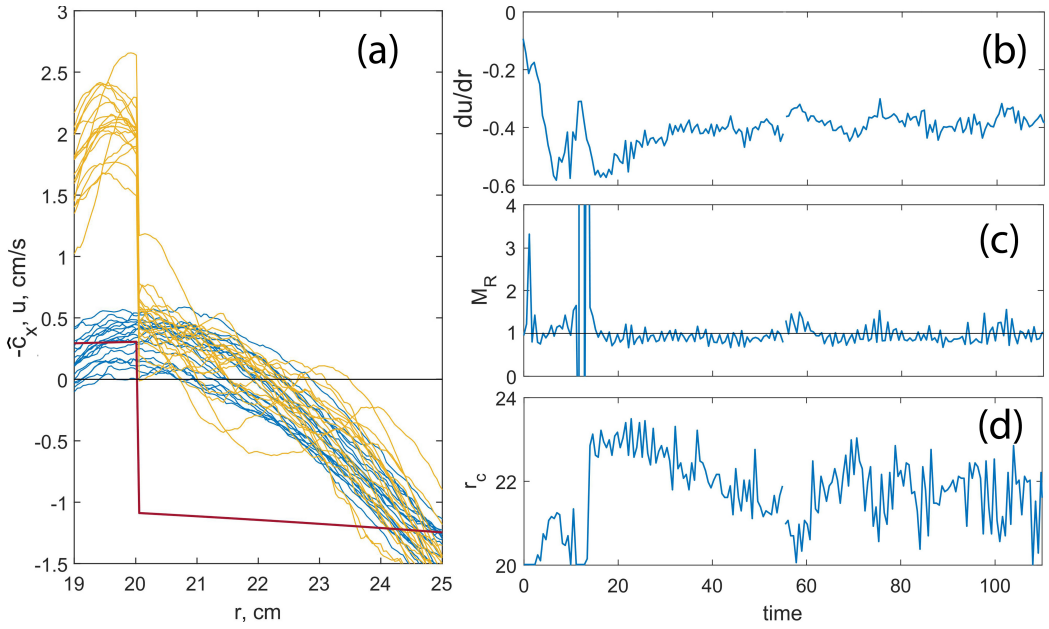

Figure 9. Zoom-in of the critical latitude in the vicinity of $r = 20\,\mathrm{cm}$ (Run 2) averaged in the 6:30 to 8 o'clock sector. Shown every 2.9 rotations during the statistically steady period are (a) $-\hat{c}_x$ (yellow) and $(u - u_{\mathrm{shift}})$ (blue), which by definition crosses zero where $-\hat{c}_x$ crosses zero. The red profile is the topography-based $-\hat{c}_x$. The right panels show time series over the entire Run 2: (b) slope of $u(r)$ at the critical latitude, (c) M_{R} computed using L'Hospital's rule (see text), and (d) radial position of the critical latitude.

Inspection of Figure 7a reveals that the yellow curves $(-\hat{c}_x)$ go through zero slightly off the exact zero of the topographic β_h at $r = 20\,\mathrm{cm}$, but instead cross at $r \approx 22\,\mathrm{cm}$. Here is where the freedom of the Galilean shift in $(\overline{u}-\alpha)$ comes into play. Recall that PV, and hence $-\hat{c}_x$, is invariant to such a shift. For cylindrical geometry, the procedure is as follows. Firstly, the position of the critical latitude, r_c, is located where $-\hat{c}_x(r_c) = 0$. Secondly, the zeroes of the numerator and denominator of M_{R}^{-1} are made to coincide by shifting to a new reference frame with angular velocity, $\Omega_{\mathrm{shift}} = u(r_c)/r_c$, and corresponding zonal velocity, $(u - u_{\mathrm{shift}})$, where $u_{\mathrm{shift}}(r) = r\Omega_{\mathrm{shift}}$. To stay in the reference frame of the circulation's critical latitude, this shift is recalculated for each time.

A zoom-in of the shifted velocity profiles for the weaker critical latitude is shown in Figure 9a. The radial derivative, du/dr at $r = r_c$ (Figure 9b), remains negative throughout the entire Run 2. Figure 9c shows a time series of $M_R = -(u - u_{\mathrm{shift}})/\hat{c}_x$ at the critical latitude, $r = r_c$. Since both the numerator and denominator tend to zero at r_c, L'Hospital's rule is used to compute M_{R} in the form $-(du/dr)(d\hat{c}_x/dr)^{-1}$. Finally, Panel (d) shows the position of the critical latitude as a function of time.

A similar analysis is made for the stronger critical latitude. Unlike for the weaker one, here the factor $d(-\hat{c}_x)/dr$ is practically infinite, such that the position of the critical latitude stays fixed at $r_c = 35$ cm throughout the runs. The velocity profiles shifted to 0 at this latitude are shown in Figure 10a, and Panel (b) shows the derivative, du/dr, as a function of time. Notice that du/dr oscillates around zero, but with some prevalence for negative (stable) values. Consequently, M_{R} is quite small and vacillates around zero in a manner consistent with a weak shear that is being continuously buffeted by forc-

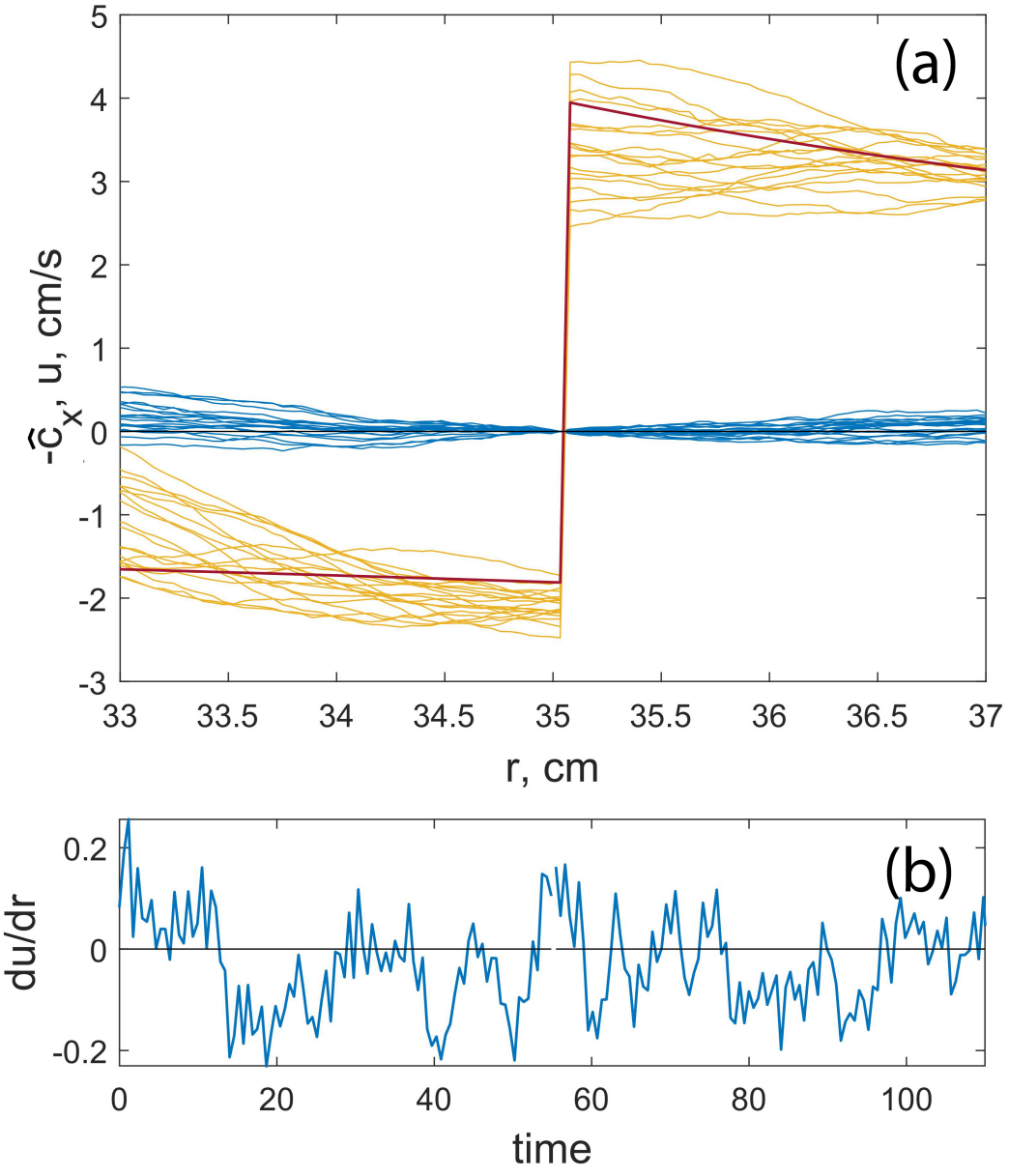

Figure 10. As in Figure 9a,b, but for the critical latitude at $r = 35\,\mathrm{cm}$.

ing (in such weak-shear situations, the reciprocal, M_{R}^{-1}, is less useful because it switches between $\pm\infty$). Unlike the other critical latitude, this one does not exhibit $M_{\mathrm{R}}^{-1} \to 1$ behavior.

4.5 Details in Zone 2

The main novelty of these experiments is the tent-shaped seamount that yields an annulus (zone) with negative β_h that is surrounded by positive β_h. There are two additional features of interest to point out for the circulations in this Zone 2. Firstly, the Rossby wave phase speed is eastward (cyclonic, prograde, counterclockwise) in Zone 2, and hence this is the only one where long Rossby waves have a chance to propagate upstream against the tank-wide westward flow (anticyclonic, retrograde, clockwise) induced by the mass-injection forcing. As shown in Figure 3c, a high-pressure β-plume propagates eastward from the forcing in Zone 2, flanked by counter-flowing zonal jets in the anticyclonic sense. When the flow achieves a mature state, both jets encircle the tank and settle into their final positions, the eastward-flowing jet at the boundary between Zones 1 and 2 at $r = 20$ cm, and the westward-flowing jet in the middle of Zone 2.

The fate of the built-in topographical critical layer at $r = 20\,\mathrm{cm}$ is in fact more complicated than just the simple translation to $r = 22\,\mathrm{cm}$ documented above: a second critical latitude develops just inside Zone 1 at $r \approx 18\,\mathrm{cm}$, as can be seen in Figure 7 (Run 2) and Figure 8a (Runs 2 and 3). The general development of M_{R}^{-1} towards unity in the region where Rossby waves propagate upstream is analogous to the choking phenomenon of hydraulics, but for Rossby waves instead of gravity waves (e.g. Armi, 1989; Dowling, 1993; Stanley et al., 2020). The lesson for the circulations on Jupiter seems to be that instead of wiping out critical latitudes ($M_{\mathrm{R}}^{-1} \to 0$), when tropospheric jets are strong enough, they can stabilize by moving and even splitting critical latitudes, preserving them via $M_{\mathrm{R}}^{-1} \sim 1$. The dynamic topography from deep jets is essential to this process, since $M_{\mathrm{R}} = 1$ in Jupiter's troposphere implies the deep jets are related to β_u calculated for the tropospheric jets, $u_{\mathrm{deep}} = (\beta + \beta_u)L_d^2 \neq 0$ (Dowling, 1993, 2020).

Secondly, there are often areas in Zone 2 where M_{R}^{-1} exceeds unity (e.g. Figures 6d and 8), which is interesting because this is necessary for shear instability. The dipolar component of the circulation discussed above causes the left and right halves of Zone 2 to be different (Figure 6d). Evidently, the dipolar circulation is blocking the propagation of $M_{\mathrm{R}}^{-1} \sim 1$ into the right half. As a result, the potentially unstable areas of high-positive M_{R}^{-1} are more extensive and the flow is more "wavy" in the right half (Figure 4c).

5 Conclusions

A rotating water tank with localized mass forcing and strong bottom topography is used to initiate laboratory studies of systems with alternating potential vorticity gradients, β_e, as motivated by observations of Jupiter and Saturn. A tent-shaped seamount that is azimuthally symmetric sets up four zones: a polar Zone 1, a negative β_e Zone 2, and two outer, positive-β_e Zones 3 and 4.

Once the water is at rest in the tank's rotating reference frame, mass injection from a submerged source pipe along one radius is turned on continuously, with the strength varied between experiments. This forcing creates alternating jets via the β-plume mechanism, which involves radiation of Rossby-wave envelopes from the forcing. Each β-plume is a region of high or low pressure, i.e. high or low surface deviation from the parabolic geoid, which grows in the zonal direction with two jets flowing in opposite directions.

Conditions in Zone 2 allow for the upwind combination of eastward propagating long Rossby waves and westward fluid velocity, such that the Rossby waves propagate

upstream over much of the zone. Hydraulic-like control of the flow takes hold and is made evident by computing the analog of the Mach (or Froude number) for Rossby waves, M_{R}, which approaches unity over much of Zone 2, with some shaping by the circulation. It is emphasized that this parameter and its reciprocal, M_{R}^{-1}, are central to a range of theories, including those pertaining to jet spacing (e.g. Rhines, 1975), hydraulic control of Rossby waves (e.g. Armi, 1989), and shear stability (e.g. Dowling, 2019), and that in all these applications, the condition $M_{\mathrm{R}} \sim 1$ is favored. In Zone 3, the environmental conditions are sufficiently different from Zone 2 that $M_{\mathrm{R}}^{-1} \sim 1$ does not develop. The mass injection causes a tank-sized westward (anticyclonic) circulation, and this circulation sweeps downstream Rossby waves generated in the forcing area of Zone 3, which is the negative M_{R}^{-1} or M_{R} case and is shear stable.

The present design of experiments provides a system with two built-in topographic critical latitudes where β_h changes sign, namely the boundaries of Zone 2. For the outer boundary positioned above the peak of the seamount, which has the stronger change in PV gradient, M_{R} vacillates about zero, with weak but persistent unsteadiness and a slight preference for negative (stable) values. This configuration may be applicable to the vicinity of oceanic seamounts. In contrast, the inner critical latitude, positioned above the poleward foot of the seamount, rapidly achieves $M_{\mathrm{R}}^{-1} \sim 1$. It is able to reconfigure itself, with a split and lateral shifts, which lends support to the idea that gas-giant tropospheres are flexible in their ability to adjust to the dynamic topography of abyssal jets.

These experiments explore the evolution of zonal flows starting from rest, and contribute to the understanding of the paths an evolving system may take towards the $M_{\mathrm{R}}^{-1} \rightarrow 1$ state. The β-plume mechanism is a feature of these experiments because of the continuous, localized forcing strategy employed. This mechanism represents only one means of forming alternating jets, but it proves to be a robust one. It can be motivated for gas giants along the following lines. Suppose there are relatively persistent sources of vortical eddies, created by moist convection and/or shear instability, which generate β-plumes via radiation of Rossby waves (in the present experiments the plumes originate in the forcing area only). Each plume consists of two counter-flowing zonal jets. Where β_e and u have the same sign, such that M_{R}^{-1} is positive and Rossby waves travel upstream and can become choked, the condition $M_{\mathrm{R}}^{-1} \rightarrow 1$ is readily established and expands to encircle the planet. On the other hand, where β_e and u have opposite signs, such that M_{R}^{-1} is negative, this circulation may be squeezed out by being continuously washed downstream, and may even jump tracks to merge into an adjacent zone.

To further test such ideas, and otherwise to advance laboratory analogies for Jupiter and Saturn, future experiments should consider modifications to this initial study with the goal of configuring a system for which: i) $M_{\mathrm{R}}^{-1} \rightarrow 1$ is possible in adjacent zones with alternating PV gradients, and ii) critical latitudes are in communication with each other regarding meridional coherence of long Rossby waves. The first design lesson from this study is that the seamount or seamounts probably do not need to be as strong (as tall) as employed here. The second lesson is that multiple seamounts are likely to succeed in producing multiple stable critical latitudes, even in a similarly sized tank, considering that alternating β-plumes developed in this study without difficulty. The third lesson is that other forms of forcing should be tried, for example a more uniform distribution of mass sources that does not produce a tank-sized anticyclone, or one of various types of thermal forcing. All of these modifications are relatively straightforward, and so the prospects for future Jupiter-in-a-tank experiments are bright.

6 Data Availability Statement

Datasets for this research are available in Y. D. Afanasyev and Dowling (2021).

Acknowledgments

YDA is supported by the Natural Sciences and Engineering Research Council of Canada.

References

Afanasyev, Y., Rhines, P., & Lindahl, E. (2008). Vorticies and Rossby waves in cylinder wakes on a parabolic β-plane observed by altimetric imaging velocimetry. *Phys. Fluids*, *20*, 086604. doi: 10.1063/1.2968451

Afanasyev, Y. D. (2015). Altimetry in a GFD laboratory and flows on the polar β-plane. In T. von Larcher & P. Williams (Eds.), *Modelling atmospheric and oceanic flows: Insights from laboratory experiments and numerical simulations* (pp. 101–117). Hoboken, New Jersey: AGU Wiley.

Afanasyev, Y. D. (2019). Turbulence, Rossby waves and zonal jets on the polar β-plane: Experiments with laboratory altimetry. In B. Galperin & P. L. Read (Eds.), *Zonal jets: Phenomenology, genesis, and physics* (pp. 152–166). New York: Cambridge Univ. Press.

Afanasyev, Y. D., & Dowling, T. E. (2021). Jupiter-style critical latitudes in the laboratory.
doi: 10.6084/m9.figshare.16438950.v1

Afanasyev, Y. D., & Ivanov, L. M. (2019). β-plume mechanism of zonal jet creation by a spatially localized forcing. In B. Galperin & P. L. Read (Eds.), *Zonal jets: Phenomenology, genesis, and physics* (pp. 266–283). New York: Cambridge Univ. Press.

Afanasyev, Y. D., & Jewtoukoff, V. (2009). Dipolar gyres generated by continuous forcing on a polar β-plane. *Physics of Fluids*, *21*, 066602.

Afanasyev, Y. D., O'Leary, S., Rhines, P. B., & Lindahl, E. G. (2012). On the origin of jets in the ocean. *Geoph. Astroph. Fluid Dyn.*, *106*, 113–137. doi: 10.1080/03091929.2011.562896

Afanasyev, Y. D., Rhines, P. B., & Lindahl, E. G. (2009). Velocity and potential vorticity fields measured by altimetric imaging velocimetry in the rotating fluid. *Exp. Fluids*, *47*, 913–926.

Antipov, S., Nezlin, M., Rodionov, V., Snezhkin, E., & Trubnikov, A. (1983). Rossby solitons: stability, collisions, asymmetry and generation by flows with velocity shear. *Sov. Phys. JETP*, *57*(4), 786–797.

Armi, L. (1989). Hydraulic control of zonal currents on a beta-plane. *Journal of Fluid Mechanics*, *201*, 357–377. doi: 10.1017/S0022112089000972

Arnol'd, V. (1966). On an a priori estimate in the theory of hydrodynamic stability. *Izvestiya Vysshikh Uchebnykh Zavedenii. Matematika*, *5*, 3–5.

Baldwin, M. P., Rhines, P. B., Huang, H.-P., & McIntyre, M. E. (2007). The jet-stream conundrum. *Science*, *315*, 467–468. doi: 10.1126/science.1131375

Balmforth, N., & Morrison, P. (1999). A necessary and sufficient instability condition for inviscid shear flow. *Studies in Applied Mathematics*, *102*, 309–344.

Balmforth, N., & Morrison, P. (2002). Hamiltonian description of shear flow. In J. Norbury & I. Roulstone (Eds.), *Large-scale atmosphere-ocean dynamics volume ii: Geometric methods and models* (pp. 117–142). New York: Cambridge Univ. Press.

Condie, S., & Rhines, P. (1994). A convective model for the zonal jets in the atmospheres of Jupiter and Saturn. *Nature*, *367*, 711—713. doi: 10.1038/367711a0

Cushman-Roisin, B., & Beckers, J.-M. (2011). *Introduction to geophysical fluid dynamics*. Academic Press.

Cushman-Roisin, B., Chassignet, E. P., & Tang, B. (1990). Westward motion of mesoscale eddies. *Journal of Physical Oceanography*, *20*, 758-768.

Darrigol, O. (2005). *Worlds of flow: a history of hydrodynamics from the Bernoullis to Prandtl*. Oxford University Press.

Davey, M. K., & Killworth, P. D. (1989). Flows produced by discrete sources of buoyancy. *J. Phys. Ocean.*, *19*, 1279–.

del Castillo-Negrete, D., & Morrison, P. (1993). Chaotic transport by Rossby waves in shear flow. *Phys. Fluids A*, *5*(4), 948–965.

Deming, D., Mumma, M. J., Espenak, F., Jennings, D. E., Kostiuk, T., Wiedemann, G., ... Piscitelli, J. (1989). A search for p-mode oscillations of Jupiter: Serendipitious observations of nonacoustic thermal wave structure. *Astrophysical Journal*, *343*, 456–467.

Dowling, T. E. (1993). A relationship between potential vorticity and zonal wind on Jupiter. *Journal of the Atmospheric Sciences*, *50*(1), 14–22. doi: 10.1175/1520-0469(1993)050⟨0014:ARBPVA⟩2.0.CO;2

Dowling, T. E. (1995a). Dynamics of Jovian atmospheres. *Annual Review of Fluid Mechanics*, *27*, 293–334.

Dowling, T. E. (1995b). Estimate of Jupiter's deep zonal-wind profile from Shoemaker-Levy 9 data and Arnol'd's second stability criterion. *Icarus*, *117*(2), 439–442. doi: https://doi.org/10.1006/icar.1995.1169

Dowling, T. E. (2014). Saturn's longitude: Rise of the second branch of shear-stability theory and fall of the first. *International Journal of Modern Physics D*, *23*, 1430006. doi: 10.1142/S0218271814300067

Dowling, T. E. (2019). Jets in planetary atmospheres. *Oxford Research Encyclopedia of Planetary Science*. doi: 10.1093/acrefore/9780190647926.013.116

Dowling, T. E. (2020). Jupiter-style jet stability. *Planetary Science Journal*, *1*(1), 6. doi: https://doi.org/10.3847/PSJ/ab789d

Dowling, T. E., Bradley, M. E., Du, J., Lewis, S. R., & Read, P. L. (2017). Ertel potential vorticity versus Bernoulli streamfunction on Mars. *Q. J. R. Meteorol. Soc.*, *143*, 37–52. doi: 10.1002/qj.2916

Dowling, T. E., & Ingersoll, A. P. (1989). Jupiter's Great Red Spot as a shallow water system. *Journal of the Atmospheric Sciences*, *46*(21), 3256-3278. doi: 10.1175/1520-0469(1989)046⟨3256:JGRSAA⟩2.0.CO;2

Du, J., Dowling, T. E., & Bradley, M. E. (2015). Ertel potential vorticity versus Bernoulli streamfunction in Earth's extratropical atmosphere. *J. Adv. Model. Earth Syst.*, *7*. doi: 10.1002/2014MS000420

Fultz, D. (1961). Developments in controlled experiments on larger scale geophysical problems. *Adv. Geophys.*, *7*, 1–103.

Galperin, B., & Read, P. L. (Eds.). (2019). *Zonal jets: Phenomenology, genesis, and physics*. Cambridge University Press.

Graney, C. M. (2010). Changes in the cloud belts of Jupiter, 1630–1664, as reported in the 1665 Astronomia Reformata of Giovanni Battista Riccioli. *Baltic Astronomy*, *19*, 265-271. doi: 10.1515/astro-2017-0425

Hart, J. E., Glatzmaier, G. A., & Toomre, J. (1986). Space-laboratory and numerical simulations of thermal convection in a rotating hemispherical shell with radial gravity. *Journal of Fluid Mechanics*, *173*, 519–544.

Hide, R. (1969). Dynamics of the atmospheres of the major planets with an appendix on the viscous boundary layer at the rigid bounding surface of an electrically-conducting rotating fluid in the presence of a magnetic field. *Journal of the Atmospheric Sciences*, *26*(5), 841-853. doi: 10.1175/1520-0469(1969)026⟨0841:DOTAOT⟩2.0.CO;2

Hirota, M., & Morrison, P. (2016). Stability boundaries and sufficient stability conditions for stably stratified, monotonic shear flows. *Physics Letters A*, *380*, 1856–1860.

Ingersoll, A. P., Beebe, R. F., Mitchell, J. L., Garneau, G. W., Yagi, G. M., & M¨ uller, J.-P. (1981). Interaction of eddies and mean zonal flow on Jupiter as inferred from Voyager 1 and 2 images. *Journal of Geophysical Research: Space Physics*, *86*(A10), 8733–8743. doi: 10.1029/JA086iA10p08733

Ingersoll, A. P., & Cuong, P. G. (1981). Numerical model of long-lived Jovian vortices. *Journal of the Atmospheric Sciences*, *38*(10), 2067-2076. doi: 10.1175/1520-0469(1981)038⟨2067:NMOLLJ⟩2.0.CO;2

Kelvin, L. (1880). Vibrations of a columnar vortex. *Phil. Mag.*, *10*, 155–168.

Kuo, H. (1949). Dynamic instability of two-dimensional non-divergent flow in a barotropic atmosphere. *Journal of Meteorology*, *6*, 105–122.

Li, L., Studwell, A., Dowling, T. E., Bradley, M. E., Creecy, E. C., Albright, R. J., & Jiang, X. (2021). Asymmetrical meridional expansion of bright clouds from Saturn's 2010 great white storm. *Icarus*, *369*, 114650. doi: 10.1016/j.icarus.2021.114650

Lin, C. C. (1945). On the stability of two-dimensional parallel flows: Part II. Stability in an inviscid fluid. *Q. Appl. Math.*, *3*(3), 218–234.

Long, R. R. (1952). The flow of a liquid past a barrier in a rotating spherical shell. *Journal of Meteorology*, *9*, 187–199.

Maas, L. R. M. (2001). Wave focusing and ensuing mean flow due to symmetry breaking in rotating fluids. *Journal of Fluid Mechanics*, *437*, 13–28.

Matulka, A. M., Zhang, Y., & Afanasyev, Y. D. (2016). Complex environmental β-plane turbulence: laboratory experiments with altimetric imaging velocimetry. *Nonlinear Processes in Geophysics*, *23*(1), 21–29. doi: 10.5194/npg-23-21-2016

McIntyre, M. E., & Shepherd, T. G. (1987). An exact local conservation theorem for finite-amplitude disturbances to non-parallel shear flows, with remarks on Hamiltonian structure and on Arnol'd's stability theorems. *Journal of Fluid Mechanics*, *181*, 527–565. doi: 10.1017/S0022112087002209

Phillips, N. A. (1965). Elementary Rossby waves. *Tellus*, *17*, 295–301.

Platzman, G. (1968). The Rossby wave. *Quarterly Journal of the Royal Meteorological Society*, *94*, 225–248.

Rabitti, A., & Maas, L. R. M. (2013). Meridional trapping and zonal propagation of inertial waves in a rotating fluid shell. *Journal of Fluid Mechanics*, *729*, 445–470.

Read, P. L. (2019). Zonal jet flows in the laboratory: An introduction. In B. Galperin & P. L. Read (Eds.), *Zonal jets: Phenomenology, genesis, and physics* (pp. 119–134). New York: Cambridge Univ. Press.

Read, P. L., Conrath, B. J., Fletcher, L. N., Gierasch, P. J., Simon-Miller, A. A., & Zuchowski, L. (2009). Mapping potential vorticity dynamics on Saturn: Zonal mean circulation from Cassini and Voyager data. *Planetary and Space Science*, *57*, 1682–1698. doi: 10.1016/j.pss.2009.03.004

Read, P. L., Dowling, T. E., & Schubert, G. (2009). Saturn's rotation period from its atmospheric planetary-wave configuration. *Nature*, *460*, 608–610.

Read, P. L., Gierasch, P. J., Conrath, B. J., Simon-Miller, A., Fouchet, T., & Yamazaki, Y. (2006). Mapping potential-vorticity dynamics on Jupiter. I: Zonal-mean circulation from Cassini and Voyager 1 data. *Quarterly Journal of the Royal Meteorological Society*, *132*, 1577–1603. doi: 10.1256/qj.05.34

Read, P. L., Sommeria, J., & Young, R. M. B. (2019). Convectively driven turbulence, Rossby waves and zonal jets: Experiments on the Coriolis platform. In B. Galperin & P. L. Read (Eds.), *Zonal jets: Phenomenology, genesis, and physics* (pp. 135–151). New York: Cambridge Univ. Press.

Rhines, P. B. (1975). Waves and turbulence on a beta-plane. *Journal of Fluid Mechanics*, *69*, 417–443. doi: 10.1017/S0022112075001504

Rogers, J., Fletcher, L., Adamoli, G., Jacquesson, M., Vedovato, M., & Orton, G. (2016). A dispersive wave pattern on Jupiter's fastest retrograde jet at 20°S. *Icarus*, *277*, 354–369. doi: https://doi.org/10.1016/j.icarus.2016.05.028

Slavin, A. G., & Afanasyev, Y. D. (2012). Multiple zonal jets on the polar beta plane. *Phys Fluids*, *24*, 113–137.

Sommeria, J., Meyers, S. D., & Swinney, H. L. (1989). Laboratory model of a planetary eastward jet. *Nature*, *337*(5), 58–61.

Stamp, A. P., & Dowling, T. E. (1993). Jupiter's winds and Arnol'd's second stability criterion: slowly moving waves and neutral stability. *Journal of Geophysical Research*, *98*(8), 847–855.

Stanley, G. J., Dowling, T. E., Bradley, M. E., & Marshall, D. P. (2020). Ertel potential vorticity versus Bernoulli potential on approximately neutral surfaces in the Antarctic Circumpolar Current. *Journal of Physical Oceanography*, *50*(9), 2621–2648. doi: https://doi.org/10.1175/JPO-D-19-0140.1

Stommel, H. M. (1982). Is the south pacific helium-3 plume dynamically active? *Earth Planet. Sci. Lett.*, *61*, 63–.

Thomson, W. (1880). On maximum and minimum energy in vortex motion. *Nature*, *22*, 618–620.

Vallis, G. K. (2017). *Atmospheric and oceanic fluid dynamics: Fundamentals and large-scale circulation* (2nd ed.). Cambridge.

Vallis, G. K., & Maltrud, M. E. (1993). Generation of mean flows and jets on a beta plane and over topography. *Journal of Physical Oceanography*, *23*, 1346—1362. doi: 10.1175/1520-0485(1993)023⟨1346:GOMFAJ⟩2.0.CO;2

White, W. B. (1971). A Rossby wake due to an island in an eastward current. *J. Phys. Ocean.*, *1*, 161–168.

Young, W. R., & Rhines, P. B. (1980). Rossby wave action, enstrophy and energy in forced mean flows. *Geophysical & Astrophysical Fluid Dynamics*, *15*, 39–52.